Jiang, Zongyu; Kujala, Pentti; Hirdaris, Spyros; Li, Fang; Mikkola, Tommi; Suominen, Mikko

The influence of waves and hydrodynamic interaction on energy-based evaluation of ice loads during a glancing impact in sea states

Published in:
Ocean Engineering

DOI:
10.1016/j.oceaneng.2024.118719

Published: 15/10/2024

Document Version
Publisher's PDF, also known as Version of record

Ocean Engineering 310 (2024) 118719

Contents lists available at ScienceDirect

Ocean Engineering

journal homepage: www.elsevier.com/locate/oceaneng

Research paper

The influence of waves and hydrodynamic interaction on energy-based evaluation of ice loads during a glancing impact in sea states

Zongyu Jiang [a,*], Pentti Kujala [a], Spyros Hirdaris [a,b], Fang Li [c], Tommi Mikkola [a], Mikko Suominen [a]

[a] Aalto University, Marine and Arctic Technology Group, 02150, Espoo, Finland
[b] Global Ship Systems Centre, ABS Hellenic SM LLC., 176 74, Athens, Greece
[c] School of Naval Architecture, Ocean & Civil Engineering, Shanghai Jiao Tong University, 200240, Shanghai, China

ARTICLE INFO

Keywords:
Ice loads
Energy-based
Hydrodynamic interaction
Waves
Glancing impact

ABSTRACT

This research investigates the effect of waves and hydrodynamic interaction on the ice loads during a glancing impact between an ice floe and a ship advancing at low speed in various sea states. An extended energy-based model is proposed for the ice loads estimation, accounting for hydrodynamic interaction through added mass and wave-induced motions, where the hydrodynamic interaction is fully involved between an advancing ship and a free-floating ice floe. The influence of sea states is investigated by calculating the added mass and motions of a ship and ice floes in six degrees of freedom under different significant wave heights and peak periods. The effect of ice floe size is analyzed by using three ice floes with different diameters. The results reveal that sea waves significantly affect ice loads by altering the relative velocity between the ship and the ice floe right before the impact. Furthermore, the influence of added mass on ice load predictions is not as pronounced as the effect of wave-induced motions. This research underscores the importance of considering hydrodynamic interactions and wave conditions in the accurate assessment of ice loads, which is crucial for the design of ice-strengthened ships and for the selection of safe speed according to sea state in ice-infested waters.

1. Introduction

Navigating ships in ice-infested waters presents significant challenges, primarily due to the collision-induced ice loads that may damage the ship's hull. In the Marginal Ice Zone (MIZ), where the sea surface is partially covered with small or medium size ice floes, sea waves can cause wave-induced motions of ships and ice floes, altering their momentum and consequently the ice loads during collision. Traditional prediction methods (Popov et al., 1967; Daley, 1999; FSICR, 2017) overlook the influence of waves and consequently overlook motions induced by waves. Therefore, exploring the effect of six degrees of freedom (DoFs) motions on ice load evaluation is crucial because accurate assessments are vital for ensuring the safety and efficiency of operations in ice-infested waters, guiding the development of ice-strengthened ship designs and operational strategies.

The methods for the evaluation of ice loads can be briefly categorized into semi-empirical methods, numerical methods, and first-principle-based methods, etc. The semi-empirical methods rely on statistical models and extensive datasets from experimental tests and in-situ measurements to develop parameterized ice load distributions (Kujala, 1994; Choi et al., 2012; Suyuthi et al., 2013; Suominen and Kujala, 2014; Rahman et al., 2015; Kotilainen et al., 2017; Suominen et al., 2017a, 2017b, 2024; Kujala et al., 2019; Li et al., 2021a, 2021b). The semi-empirical methods utilize simplified physical models that make certain assumptions about ice properties and collision mechanics to predict ice loads (Barooni et al., 2022). One notable simplified mechanism is based on the principle of energy conservation, where the change of kinetic energy in both ship and ice is fully consumed by the work of ice loads (Popov et al., 1967; Daley, 1999). Another simplification is that the nominal contact area and average pressure in this area are often utilized to calculate the ice loads (Daley, 1999; Dolny, 2018; Kim and Tsuprik, 2018), despite the discrete high-pressure zones in the contact area (Riska et al., 1990; Muhonen, 1991; Jordaan, 2001; Taylor et al., 2019) and the decrease of pressure with the increase of the contact area (Masterson et al., 2007). The numerical methods have been extensively adopted to the analysis of ship-ice interactions because they are more

* Corresponding author.
E-mail address: zongyu.jiang@aalto.fi (Z. Jiang).

https://doi.org/10.1016/j.oceaneng.2024.118719
Received 4 April 2024; Received in revised form 10 July 2024; Accepted 11 July 2024
Available online 16 July 2024

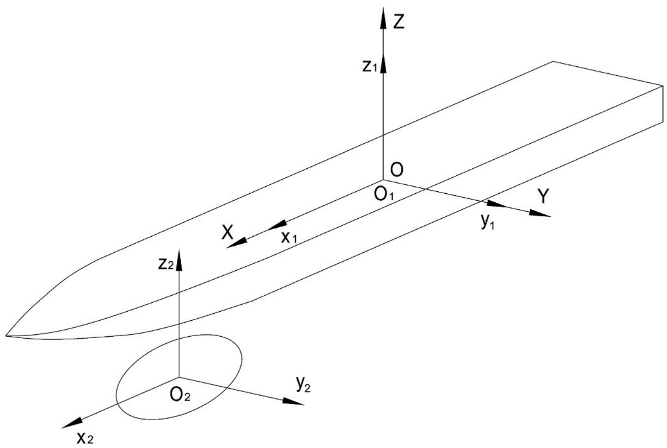

Fig. 1. Global and local coordinate systems.

accessible than testing facilities. The development of numerical methods has offered various approaches, including Finite Element Method (Li et al., 2020; Xu et al., 2020, 2022), Discrete Element Method (Polojärvi et al., 2015; Di et al., 2017; Ranta and Polojärvi, 2019; Long et al., 2020; Ji and Yang, 2022), and Cohesive Element Method (Hilding et al., 2011; Lu et al., 2014; Patil et al., 2021). Each of these methods has advantages and disadvantages, contributing uniquely to understanding and predicting ice loads. Thus, all of them offer a range of tools for researchers and engineers working on ice-strengthened ship designs and operations in ice-infested waters.

However, these research efforts largely focus on ice failure processes and structural responses, with limited consideration for the hydrodynamic effects on ship-ice interaction, particularly the absence of ship and ice hydrodynamic interaction consideration. Traditional methods, such as the one proposed by Popov et al. (1967), account for the added mass of ship and ice using oversimplified empirical formulas, neglecting the influence of geometry and sea waves on the added mass evaluation. In addition, wave-induced motions and ship-ice hydrodynamic interactions are also overlooked, despite the established effect of geometry and sea waves on marine dynamics for decades (Newman, 2018). Ommani et al. (2018) demonstrated that the added mass could significantly increase in sway due to hydrodynamic interactions between ship and ice, suggesting that these interactions are more critical than previously acknowledged. In recent years, there has been a shift towards incorporating ship motions into the evaluation of ship-ice interactions, with researchers like Su et al. (2010, 2011) and Tan et al. (2013) making notable contributions. Lu et al. (2021) developed a numerical model to calculate the first order and mean drift motions of small glacial ice, aiming to enhance ice load evaluations by considering the design kinetic energy. Yoon et al. (2023) investigated the motion and structural damage occurring during a ship-ice collision by combining potential flow theory with finite element analysis. Yet, these models still do not incorporate hydrodynamic interaction, representing a complex Fluid-Structure Interaction (FSI) challenge. Particularly, the ship's advance speed greatly increases the difficulty because the different speeds of ship and ice induce different boundary conditions in way of the free surface for the moving ship and free-floating ice. Addressing this gap, Jiang et al. (2022, 2023) introduced a novel potential flow model capable of managing the diverse free surface boundary conditions through linear superposition and the encounter frequency method. This advancement enables the incorporation of hydrodynamic interactions into the evaluation of ice loads resulting from ship-ice impacts.

The present research aims to investigate the hydrodynamic effect on the evaluation of ice loads due to glancing impacts between a ship and small to medium-sized ice floes, focusing particularly on the influence of sea waves and hydrodynamic interaction between the two bodies. Utilizing the model developed by Jiang et al. (2023), this research calculates the added mass and six degrees of freedom motions of both the ship and ice, incorporating these into an energy-based method. This approach facilitates the estimation of ice loads resulting from the glancing impact between an ice floe and a ship moving at low speed across various sea states characterized by differing significant wave heights and peak periods. Main findings reveal that the sea waves can alter the ice loads by changing the relative velocity immediately before the glancing impact. While sea waves also influence added mass, their effect on ice load predictions is less pronounced than that of wave-induced motions. In addition, the proposed approach is verified by the conventional Popov method because of its maturity for evaluating ice loads (Daley, 1999, 2000; Dolny, 2018; Idrissova et al., 2019; Zhang, 2019). This investigation is specifically focused on the glancing impacts between a ship and small to medium-sized ice floes. The primary objective is to predict the amplitude of ice loads, which have the potential to damage the ship's hull. Consequently, aspects such as ice resistance and ship speed post-impact are not considered within the scope of this research.

Subsequent to this introduction, Section 2 outlines the theoretical formulations of the numerical model. Section 3 details the case study, which involves a single ship and three ice floes of varying diameters, to analyze the size effect of the ice floes. Section 4 presents the findings and discussions. Finally, the conclusions are drawn in Section 5.

2. Method

The coordinate system comprises a global framework and two local coordinate systems fixed to the ship and ice, respectively, paralleling to the global system, as depicted in Fig. 1. The global coordinate system, denoted as O(X, Y, Z), is stationary relative to the Earth and overlaps with the ship-fixed Cartesian reference point, $O_1(x_1, y_1, z_1)$, where x_1 represents the forward direction, y_1 the port side, and z_1 upward direction. The system's origin, O_1, is positioned amidships on the mean free surface. Parallel to the ship-fixed system, the ice-fixed Cartesian coordinate system, O_2 (x_2, y_2, z_2), places its origin, O_2, at the ice floe's horizontal center and also situated on the mean free surface.

2.1. Hydrodynamic interaction

The potential flow theory considers the fluid inviscid and irrotational, therefore the velocity of fluid point can be expressed with the gradient of potential ϕ. Thus, the mass conservation of incompressible fluid can be described with Laplace equation

$$\nabla^2\phi = \frac{\partial\phi^2}{\partial x^2} + \frac{\partial\phi^2}{\partial y^2} + \frac{\partial\phi^2}{\partial z^2} = 0 \tag{1}$$

Based on the linear superposition principle, when only one ship and one ice floe is considered in the multibody system, the potential of ship-ice system can be expressed (Jiang et al., 2023)

$$\phi = \sum_{m=1}^{2}\sum_{j=1}^{6}\left(-i\omega\eta_j^m\phi_j^m\right) + a_0\left(\phi_0 + \sum_{m=1}^{2}\phi_7^m\right) \tag{2}$$

where the upper script m is the body's serial number ($m = 1$ represents the ship and $m = 2$ represents the ice floe), ω is the wave frequency, η_j^m is the j-mode motion amplitude of body m, ϕ_j^m is the corresponding radiation potential, a_0 is the amplitude of incoming waves, ϕ_0 is the potential of incoming waves, ϕ_7^m is the scattering potential of m^{th} body. Following the above superposition of velocity potential, the radiation of the multibody system can be expressed as

$$a_{kj} + \frac{i}{\omega}b_{kj} = -\rho \int\limits_{\sum_{m=1}^{2} S^m} \sum_{m=1}^{2}\phi_j^m \sum_{m=1}^{2}\frac{\partial\phi_k^m}{\partial n}dS \quad \text{for } k,j = 1,2,\cdots,6 \tag{3a}$$

$$a_{kj}+\frac{i}{\omega}b_{kj}=-\rho\int_{S^1}\frac{\partial\phi_k^1}{\partial n}\phi_j^1 dS-\rho\int_{S^1}\frac{\partial\phi_k^1}{\partial n}\phi_j^2 dS-\rho\int_{S^2}\frac{\partial\phi_k^2}{\partial n}\phi_j^1 dS$$
$$-\rho\int_{S^2}\frac{\partial\phi_k^2}{\partial n}\phi_j^2 dS=a_{kj}^{11}+a_{kj}^{12}+a_{kj}^{21}+a_{kj}^{22}+\frac{i}{\omega}\left(b_{kj}^{11}+b_{kj}^{12}+b_{kj}^{21}+b_{kj}^{22}\right) \quad (3b)$$

where a_{kj} and b_{kj} are respectively the added mass and damping, S^m is the wetted surface of m^{th} body, n represents the normal vector of wetted surface positively pointing inward the fluid domain.

Herein, the encounter frequency method is introduced to deal with the ship's advancing speed

$$\omega_e=\omega-kU\cos\theta \quad (4)$$

Where ω_e is the encounter frequency, $k=\omega^2/g$ is the wavenumber, g is the acceleration of gravity, θ is the propagating angle of waves. Within the encounter frequency method, only the radiation potentials in pitch and yaw are considered speed-dependent

$$\phi_j=\phi_j^0, j=1,2,3,4 \quad (5a)$$

$$\phi_5=\phi_5^0+\frac{U}{i\omega_e}\phi_3^0 \quad (5b)$$

$$\phi_6=\phi_6^0-\frac{U}{i\omega_e}\phi_2^0 \quad (5c)$$

Thus, the added mass and damping of ship and ice floe can be expressed

$$a_{kj}^{12}=a_{kj}^{12-0}, b_{kj}^{12}=b_{kj}^{12-0} \quad k=1,2,3,4 \quad j=1,2,\cdots,6 \quad (6a)$$

$$a_{kj}^{21}=a_{kj}^{21-0}, b_{kj}^{21}=b_{kj}^{21-0} \quad k=1,2,\cdots,6 \quad j=1,2,3,4 \quad (6b)$$

$$a_{5j}^{12}+\frac{i}{\omega}b_{5j}^{12}=-\rho\int_{S^1}\frac{\partial\phi_5^{1-0}}{\partial n}\phi_j^{2-0}dS-\frac{U}{i\omega_e^1}\rho\int_{S^1}\frac{\partial\phi_3^{1-0}}{\partial n}\phi_j^{2-0}dS \quad j=1,2,\cdots,6 \quad (6c)$$

$$a_{6j}^{12}+\frac{i}{\omega}b_{6j}^{12}=-\rho\int_{S^1}\frac{\partial\phi_6^{1-0}}{\partial n}\phi_j^{2-0}dS+\frac{U}{i\omega_e^1}\rho\int_{S^1}\frac{\partial\phi_2^{1-0}}{\partial n}\phi_j^{2-0}dS \quad j=1,2,\cdots,6 \quad (6d)$$

$$a_{k5}^{21}+\frac{i}{\omega}b_{k5}^{21}=-\rho\int_{S^2}\frac{\partial\phi_k^{2-0}}{\partial n}\phi_5^{1-0}dS-\frac{U}{i\omega_e^1}\rho\int_{S^2}\frac{\partial\phi_k^{2-0}}{\partial n}\phi_3^{1-0}dS \quad k=1,2,\cdots,6 \quad (6e)$$

$$a_{k6}^{21}+\frac{i}{\omega}b_{k6}^{21}=-\rho\int_{S^2}\frac{\partial\phi_k^{2-0}}{\partial n}\phi_6^{1-0}dS+\frac{U}{i\omega_e^1}\rho\int_{S^2}\frac{\partial\phi_k^{2-0}}{\partial n}\phi_2^{1-0}dS \quad k=1,2,\cdots,6 \quad (6f)$$

where the upper script 0 indicates the potential induced by the body without advancing speed.

In the scenario of a ship passing by an ice floe, the motions of these two bodies can be expressed as

$$\begin{bmatrix} M_{kj}^{11}+a_{kj}^{11} & a_{kj}^{12} \\ a_{kj}^{21} & M_{kj}^{22}+a_{kj}^{22}\end{bmatrix}\begin{Bmatrix}\ddot{x}_j^1\\ \ddot{x}_j^2\end{Bmatrix}+\begin{bmatrix} b_{kj}^{11} & b_{kj}^{12} \\ b_{kj}^{21} & b_{kj}^{22}\end{bmatrix}\begin{Bmatrix}\dot{x}_j^1\\ \dot{x}_j^2\end{Bmatrix}+\begin{bmatrix} C_{kj}^{11} & 0 \\ 0 & C_{kj}^{22}\end{bmatrix}\begin{Bmatrix}x_j^1\\ x_j^2\end{Bmatrix}$$
$$=\begin{Bmatrix}F_k^1\\ F_k^2\end{Bmatrix} k,j=1,2,\cdots,6 \quad (7)$$

where M is the mass of ship or ice, x_j is the displacement of j-mode motion, C is the hydrostatic stiffness of ship or ice, $F_k^m=-i\omega\rho a_0\int_{S^m}(\phi_0+\phi_7^m)n_k dS$ is the wave loads.

2.2. Added mass and wave induced motions in short term sea state

Section 2.1 introduces frequency domain analysis, which generates the Response Amplitude Operator (RAO) concerning wave frequency in regular waves. However, actual sea conditions are irregular, which can be decomposed into countless regular waves of varying heights and periods. Unlike direct wave loads, waves do not directly influence ice loads during a glancing impact. Instead, waves first alter the added mass and motions of both the ship and the ice floe. These changes subsequently influence the kinetic energy absorbed during the impact by the ice load and finally alter the ice loads. This process differs significantly from the dynamics of wave loads in irregular waves. It is presumed that contribution of every regular wave with specific frequency and height in a spectrum of irregular waves is equally considered in the evaluation of added mass and wave-induced motions. Consequently, the stochastic mean of added mass and motions within a sea state is utilized in the energy-based evaluation of ice loads.

$$\left.\begin{aligned} m_0 &= \int_0^\infty S(\omega)|a(\omega)|^2 d\omega \\ a_{mean} &= \sqrt{2\pi m_0}\end{aligned}\right\} \quad (8)$$

where m_0 is the zero moment of response spectrum; $S(\omega)$ is the wave energy spectrum; $a(\omega)$ is the transfer function; a_{mean} is the stochastic mean.

2.3. Energy-based ice loads evaluation

Popov et al. (1967) introduced a method for evaluating ice loads during ship-ice collisions, involving two phases: 1) Phase I applies momentum conservation to determine the reduced mass and reduced velocity, facilitating the calculation of the ship-ice system's kinetic energy; 2) Phase II employs energy conservation, assuming the kinetic energy is entirely absorbed by the ice load's work during the process of crushing, thereby estimating the ice load's amplitude and its displacement (crushing depth) using the principle of least action. However, the Popov method simplifies the hydrodynamic effect during ship-ice collisions, notably neglecting wave-induced motions and considering only the ship's forward speed in Phase I. This study integrates wave-induced motions into the reduced velocity evaluation of the ship and ice, incorporating hydrodynamic interactions through the model outlined in Section 2.1. Furthermore, the added mass used in ice load calculations is derived from the same model, enhancing the method's accuracy by including hydrodynamic effects. According to the research of Jiang et al. (2024), the used added mass should be $a_{ij}=a_{kj}^{11}+a_{kj}^{12}$ for the ship and $a_{2\_ij}=a_{kj}^{21}+a_{kj}^{22}$ for the ice floe since both ship and ice oscillate in waves. Therefore, utilizing the law of momentum conservation, the subsequent formulas facilitate the calculation of reduced velocity and reduced mass, for the ship

$$\left.\begin{aligned} (M_1+a_{11})(v_1-v_0)&=-l_1 S \\ (M_1+a_{22})(u_1-u_0)&=-m_1 S \\ (M_1+a_{33})(w_1-w_0)&=-n_1 S \\ (I_x+a_{44})(p_1-p_0)&=-\lambda_1 S \\ (I_y+a_{55})(q_1-q_0)&=-\mu_1 S \\ (I_z+a_{66})(r_1-r_0)&=-\nu_1 S\end{aligned}\right\} \quad (9)$$

for the ice floe

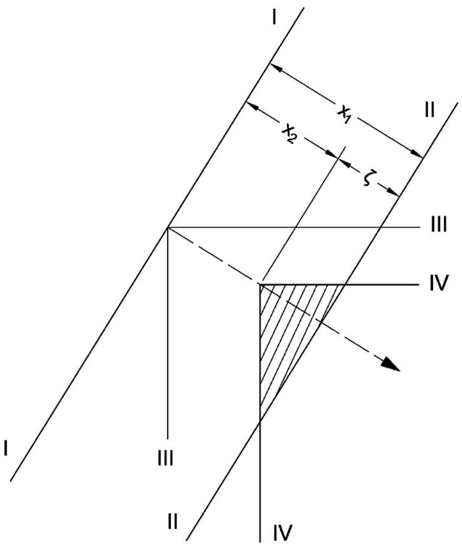

Fig. 2. The ice crushing indentation during the impact, I–I is the hull position at start of impact, II-II is the hull position during impact, III-III is the ice position at start of impact, IV-IV is the ice position during impact.

Table 1
Mian dimensions of ship.

Item [unit]	Value
Length, L_{oa} [m]	164.4
Breadth, B [m]	21.5
Draft, T [m]	9.5
Volume of displacement, $\nabla[m^3]$	2.2E+4
Center of gravity above base, $\overline{KG}$ [m]	12.8
Radius of inertia for roll, k_{xx} [m]	7.0
Radius of inertia for pitch/yaw, k_{yy}/ k_{zz} [m]	37.5
Waterline angle at impact point, α [degree]	26.5
Frame angle at impact point, β [degree]	40.6

$$\left.\begin{array}{c}(M_2+a_{2\_11})(v_2-v_{02})=l_2S\\(M_2+a_{2\_22})(u_2-u_{02})=m_2S\\(M_2+a_{2\_33})(w_2-w_{02})=n_2S\\(I_{x2}+a_{2\_44})(p_2-p_{02})=\lambda_2S\\(I_{y2}+a_{2\_55})(q_2-q_{02})=\mu_2S\\(I_{z2}+a_{2\_66})(r_2-r_{02})=\nu_2S\end{array}\right\} \tag{10}$$

where M_1 and M_2 are the mass of ship and ice floe, respectively; S is the impact momentum; I_x, I_y, I_z are the moments of inertia of ship in roll, pitch, and yaw, respectively; I_{x2}, I_{y2}, I_{z2} are the moments of inertia of ice in roll, pitch, and yaw, respectively; v_0, u_0, w_0, p_0, q_0, r_0 are the velocity of ship before impact in surge, sway, heave, roll, pitch, and yaw, respectively (note that v_0 involves the ship's advancing speed); v_1, u_1, w_1, p_1, q_1, r_1 are the velocity of ship after impact in surge, sway, heave, roll, pitch, and yaw, respectively; v_{02}, u_{02}, w_{02}, p_{02}, q_{02}, r_{02} are the velocity of ice floe before impact in surge, sway, heave, roll, pitch, and yaw, respectively; v_2, u_2, w_2, p_2, q_2, r_2 are the velocity of ice floe after impact in surge, sway, heave, roll, pitch, and yaw, respectively; l_1, m_1, n_1 are the cosine of angle between the norm of hull surface at the impact point and the axes of O_1x_1, O_1y_1, O_1z_1, respectively; l_2, m_2, n_2 are the cosine of angle between the norm of hull surface at the impact point and the axes of O_2x_2, O_2y_2, O_2z_2, respectively; $\lambda_1 = y_1n_1 - z_1m_1$, $\mu_1 = z_1l_1 - x_1n_1$, $\nu_1 = x_1m_1 - y_1l_1$ are the moment arms of impact momentum in roll, pitch, and yaw for the ship, respectively; $\lambda_2 = y_2n_2 - z_2m_2$, $\mu_2 = z_2l_2 - x_2n_2$, $\nu_2 = x_2m_2 - y_2l_2$ are the moment arms of impact momentum in roll, pitch, and yaw for the ice, respectively; x_1, y_1, z_1 are coordinates of impact point on ship; x_2, y_2, z_2 are coordinates of impact point on ice.

Assuming that the velocities of ship and ice becomes equal in the impact direction at the end of impact, the following formula can be obtained

$$\begin{aligned}&l_1v_1+m_1u_1+n_1w_1+(q_1z_1-r_1y_1)l_1+(r_1x_1-p_1z_1)m_1+(p_1y_1\\&\quad-q_1x_1)n_1=l_2v_2+m_2u_2+n_2w_2+(q_2z_2-r_2y_2)l_2+(r_2x_2-p_2z_2)m_2\\&\quad+(p_2y_2-q_2x_2)n_2\end{aligned} \tag{11}$$

Jointly solving equations (9)–(11), the impact momentum can be obtained

$$S=\frac{v_{red}}{\frac{C_1}{M_1}+\frac{C_2}{M_2}} \tag{12}$$

where v_{red} is the reduced velocity; C_1 and C_2 are the coefficients for the reduced mass of ship and ice, respectively.

$$\begin{aligned}v_{red}&=l_1v_0+m_1u_0+n_1w_0+\mu_1q_0+\nu_1r_0+\lambda_1p_0\\&\quad-(l_2v_{02}+m_2u_{02}+n_2w_{02}+\mu_2q_{02}+\nu_2r_{02}+\lambda_2p_{02})\end{aligned} \tag{13}$$

$$C_1=\frac{l_1^2}{M_1+a_{11}}+\frac{m_1^2}{M_1+a_{22}}+\frac{n_1^2}{M_1+a_{33}}+\frac{\lambda_1^2}{I_x+a_{44}}+\frac{\mu_1^2}{I_y+a_{55}}+\frac{\nu_1^2}{I_z+a_{66}} \tag{14}$$

$$\begin{aligned}C_2&=\frac{l_2^2}{M_2+a_{2\_11}}+\frac{m_2^2}{M_2+a_{2\_22}}+\frac{n_2^2}{M_2+a_{2\_33}}+\frac{\lambda_2^2}{I_{x2}+a_{2\_44}}+\frac{\mu_2^2}{I_{y2}+a_{2\_55}}\\&\quad+\frac{\nu_2^2}{I_{z2}+a_{2\_66}}\end{aligned} \tag{15}$$

The reduced mass of ship-ice system can be expressed as

$$M_{red}=\frac{1}{\frac{C_1}{M_1}+\frac{C_2}{M_2}}=\frac{M_{1red}M_{2red}}{M_{1red}+M_{2red}} \tag{16}$$

where $M_{1red}=M_1/C_1$ and $M_{2red}=M_2/C_2$ are the reduced mass of ship and ice, respectively.

By using the reduced mass and velocity, the kinetic energy of ship and ice, consumed by the work of ice load, W, can be expressed as

$$\left.\begin{array}{l}T_{1red}=\dfrac{M_{1red}v_{red}^2}{2}\\T_{2red}=\dfrac{M_{2red}v_{red}^2}{2}\\W=\displaystyle\int_0^{\zeta}Fd\zeta\end{array}\right\} \tag{17}$$

where T_{1red} is the ship's kinetic energy consumed by ice crushing, T_{2red} is the ice's kinetic energy consumed by ice crushing, F is the contact crushing force; ζ is the maximum crushing indentation, see Fig. 2.

Based on the principle of least action, the integral of Lagrangian function, $L = T_{1red} + T_{2red} - W$, over time must be minimum

$$I(\zeta,x_1)=\int_0^t\left[\frac{M_{1red}\dot{x}_1^2}{2}+\frac{M_{2red}(\dot{x}_1-\dot{\zeta})^2}{2}-\int_0^{\zeta}Fd\zeta\right]dt=min \tag{18}$$

Euler's equations must be satisfied to reach the minimum $I(\zeta, x_1)$, leading to a differential equation to determine the crushing indentation and the contact force

$$M_{1red}\ddot{\zeta}=-F\left(1+\frac{M_{1red}}{M_{2red}}\right) \tag{19}$$

If the contact force F is defined as the integral of crushing strength of ice, σ_c, over the contact area, the contact force can be expressed

$$F=\int\sigma_c dP \tag{20}$$

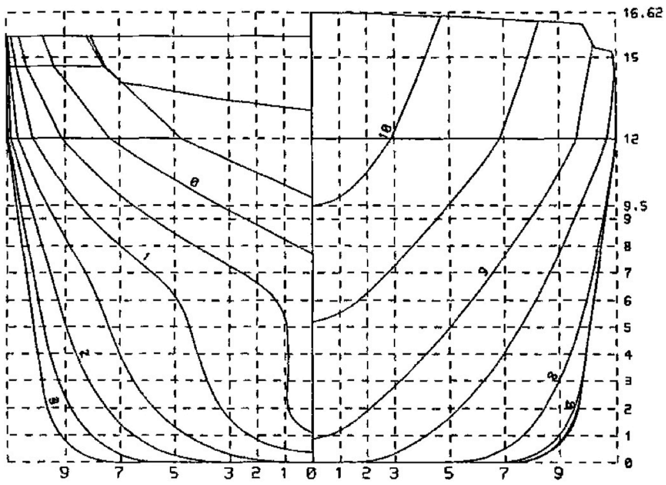

Fig. 3. Outline of the ship.

where $P = A\zeta^a$ is the contact area; A and a are two coefficients depending on the geometry of ice floe's edge at the collision point. By introducing the initial conditions, the maximum crushing indentation and contact force (ice load) can be obtained

$$\zeta_{max} = \left(\frac{(1+a)M_{red}v_{red}^2}{2A\sigma_c}\right)^{\frac{1}{1+a}} \tag{21}$$

$$F_{max} = A\sigma_c\left(\frac{(1+a)M_{red}v_{red}^2}{2A\sigma_c}\right)^{\frac{a}{1+a}} \tag{22}$$

3. Model setup

3.1. Main dimensions of ship hull and ice floe

This study calculates ice loads resulting from a glancing impact between an ice-class oil tanker, cruising at 5 knots ($F_n = 0.07$), and three ice floes. The tanker's principal dimensions are detailed in Table 1, with its line drawing depicted in Fig. 3. The impact location is $x_1 = 67.7m$, $y_1 = 5.0m, z_1 = 0.2m$ in the ship-fixed coordinate system. The ice floes, modeled as circular discs with a uniform thickness of 2 m, vary in diameter from $0.3L_{oa}$ to $0.9L_{oa}$ in increments of $0.3L_{oa}$. This variation in size allows for the examination of how different-sized ice floes react to sea waves and the hydrodynamic effects of the ship, thereby illustrating the size effect on ice loads. Given the circular disc shape of the ice floes, their geometric coefficients can be determined (Popov et al., 1967)

$$\left.\begin{aligned} a &= 1.5 \\ A &= \frac{4}{3}\frac{\sqrt{2R}}{\cos^{1.5}\beta' \sin\beta'} \end{aligned}\right\} \tag{23}$$

where R is the radius of ice floe; β' is the normal frame angle, $\tan\beta' = \tan\beta\cos\alpha$; α and β are the waterline angle and frame angle at impact point, respectively. The compressive strength of sea ice exhibits significant variability due to many influencing factors (Weeks, 1967). In this research, the chosen compressive strength, $\sigma_c = 2.94$ MPa, falls within the range reported by Weeks (1967) and Wang et al. (2018).

3.2. Wave conditions

In the frequency domain simulation, the regular wave frequencies ω

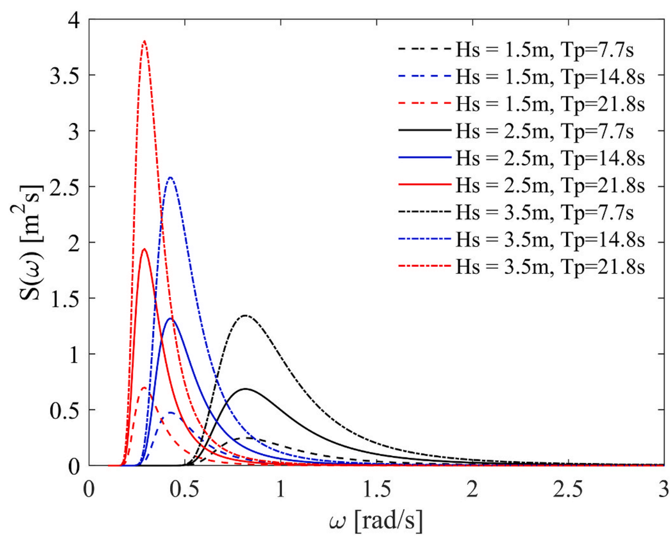

Fig. 5. Pierson-Moskowitz wave spectrum employed in the present research.

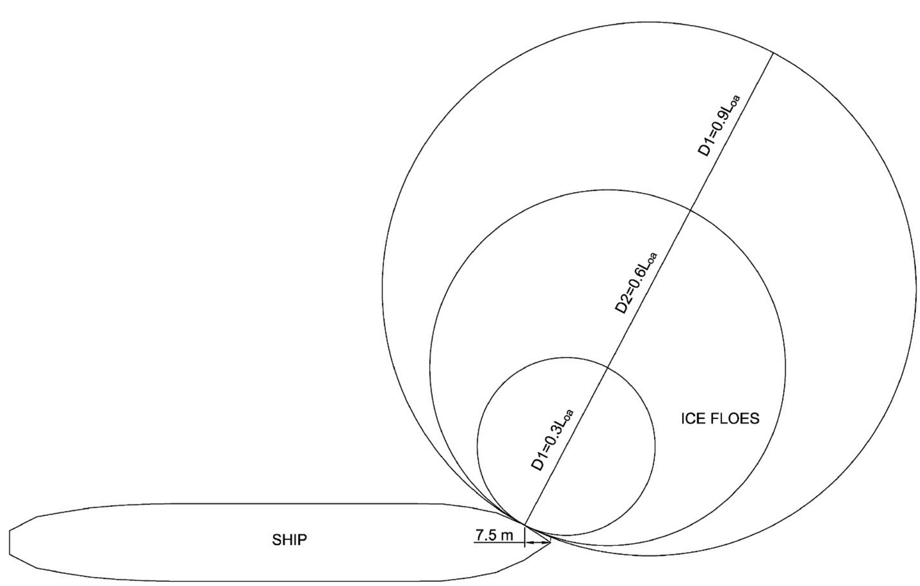

Fig. 4. Scheme of ship and ice floes in the glancing impact.

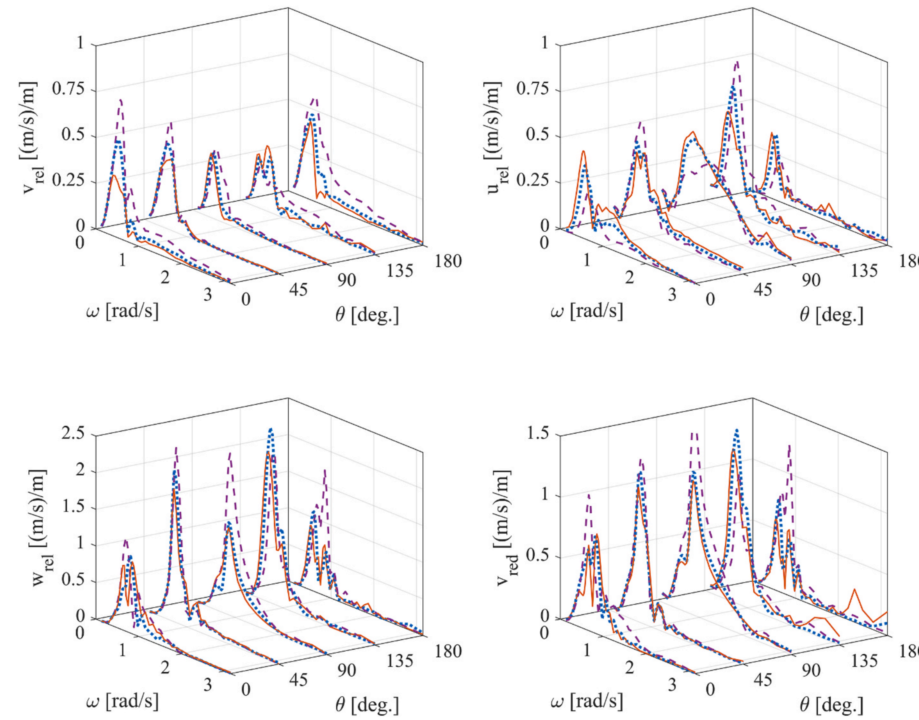

Fig. 6. RAO of relative velocity in line of impact (reduced velocity) and its components in X, Y, Z directions at impact point, dashed curves indicate the small ice floe, $D_i = 0.3L_{oa}$, dotted curves indicate the medium ice floe, $D_i = 0.6L_{oa}$, solid curves indicate the large ice floe, $D_i = 0.9L_{oa}$.

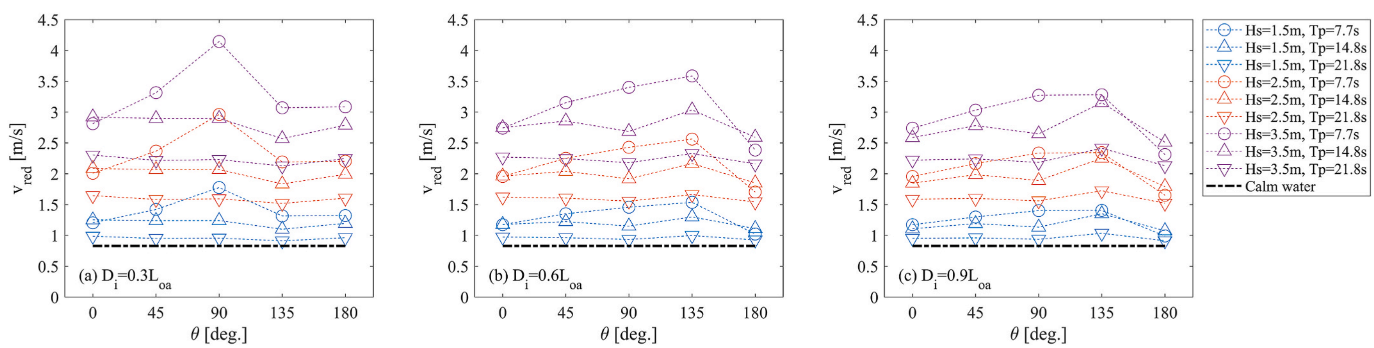

Fig. 7. Mean of reduced velocity at various sea states.

Table 2
The empirical formulas for the evaluation of added mass (Dolny, 2018).

Added mass coefficients	Ship	Ice
Surge	0	0.05
Sway	$2T/B$	0.05
Heave	$\frac{2}{3}\frac{B}{T}\frac{C_{wp}}{C_b}\frac{C_{wp}}{1+C_{wp}}$	1
Roll	0.25	1
Pitch	$\frac{B}{T(3-2C_{wp})(3-C_{wp})}$	1
Yaw	$0.3+\frac{0.05L}{B}$	0.05

ranges from 0.13 rad/s to 3.15 rad/s with wave directions θ spanning from 0° to 180° in increments of 45°. The 0° corresponds to waves propagating in the direction of the ship's forward movement, whereas a direction of 90° signifies waves propagating from the starboard to the portside of the ship. Three wave heights ($H = 1.5m, 2.5m, 3.5m$) are employed for the calculation of ice loads in regular waves. Fig. 4 illustrates the configuration of the ship-ice during a glancing impact, identifying the diameters of the ice floes as D_1, D_2, and D_3.

The literature review reveals the challenge in obtaining a fully developed wave spectrum specifically for ice-infested waters. The wave conditions in the Marginal Ice Zone (MIZ) are complex, influenced by dynamic interactions between waves and various ice characteristics like floe size and concentration, as discussed by Alberello et al. (2022) and Passerotti et al. (2022). Passerotti et al.'s experimental work also revealed that the edge of continuous ice cover significantly affects wave behavior. Therefore, the Pierson-Moskowitz (P-M) spectrum is utilized to characterize the energy distribution of sea waves in short-term sea states. The Pierson-Moskowitz spectrum is defined by the following formula

$$S_{PM}(\omega)=\frac{5}{16}H_s^2\omega_p^4\omega^{-5}\,exp\left(-\frac{5}{4}\left(\frac{\omega}{\omega^p}\right)^{-4}\right) \tag{24}$$

where ω is the wave frequency, H_s is the significant wave height, ω_p is the peak frequency of the spectrum. Thus, the spectral peak period can be expressed as $T_p = 2\pi/\omega_p$. Cheng et al. (2017) reported a dataset of sea wave observations in a marginal ice zone. According to their observation, three significant wave heights are selected ($H_s = 1.5m, 2.5m, 3.5m$)

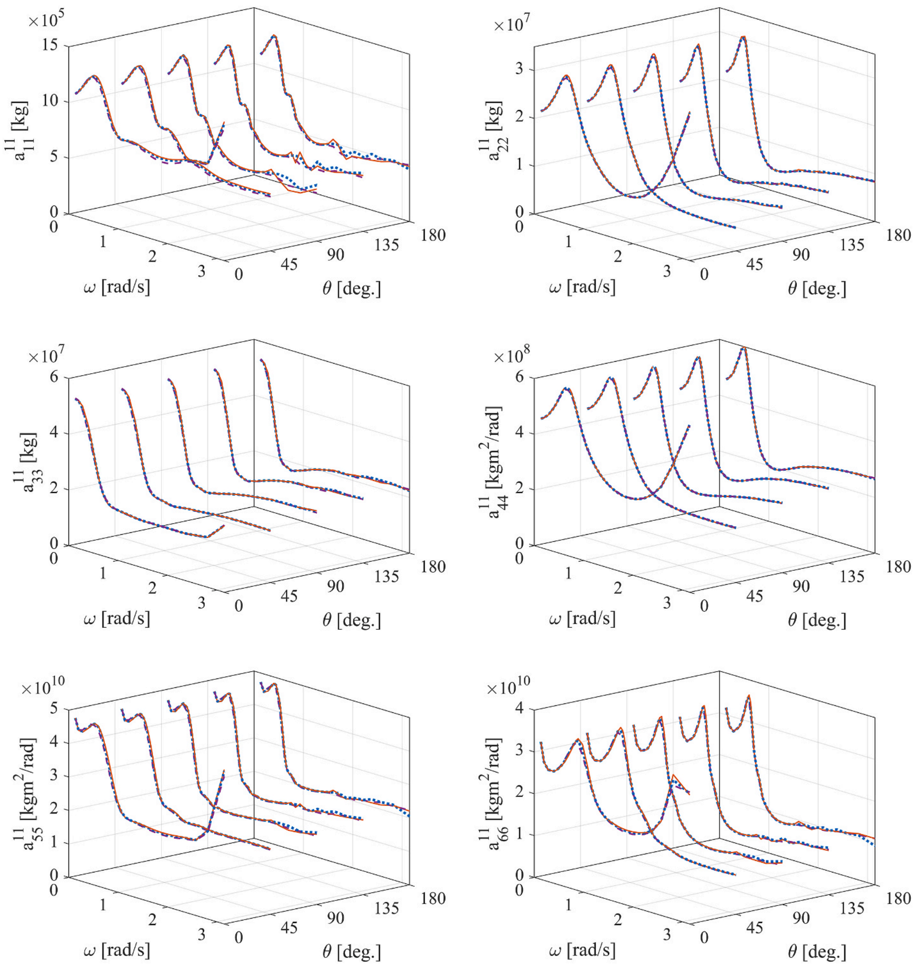

Fig. 8. RAO of ship's added mass induced by its own oscillation in six DoFs, dashed curves indicate the small ice floe, $D_i = 0.3L_{oa}$, dotted curves indicate the medium ice floe, $D_i = 0.6L_{oa}$, solid curves indicate the large ice floe, $D_i = 0.9L_{oa}$.

while the selection of three peak periods ($T_p = 7.7s, 14.8s, 21.8s$) is based on the scatter diagram for the North Atlantic (Det Norske Veritas, 2019). This selection leads to nine short-term sea states, with their corresponding Pierson-Moskowitz (P-M) wave spectra depicted in Fig. 5.

4. Results and discussion

The energy-based method assesses ice loads by quantifying the kinetic energy expended in the ice crushing process, derived from the mass, added mass, and alteration in relative velocity in the direction of impact. Hence, the relative velocity and added mass are firstly outlined, followed by a discussion of the influence of sea waves and hydrodynamic interaction. Subsequently, the variation of ice loads across different sea states is analyzed, illustrating how these factors influence ice load estimations. The hydrodynamic interaction model, used to calculate added mass and wave-induced motions of both ship and ice floe, has been rigorously examined and verified by Jiang et al. (2023). Furthermore, the ice load evaluation has been verified through comparisons with the Popov method, ensuring the reliability of our findings.

4.1. Relative velocity between ship and ice

Since the ship-fixed Cartesian reference point, $O_1(x_1, y_1, z_1)$, is parallel to the ice-fixed Cartesian reference point, $O_2(x_2, y_2, z_2)$, in this research,

$$\left.\begin{array}{c} l = l_1 = l_2 \\ m = m_1 = m_2 \\ n = n_1 = n_2 \end{array}\right\} \tag{25}$$

Thus, the reduced velocity at the impact point can be expressed as

$$\begin{aligned} v_{red} = {} & l[(v_0 - y_1 r_0 + z_1 q_0) - (v_{02} - y_2 r_{02} + z_2 q_{20})] + m[(u_0 + x_1 r_0 - z_1 p_0) \\ & - (u_{02} + x_2 r_{02} - z_2 p_{02})] + n[(w_0 - x_1 q_0 + y_1 P_0) - (w_{02} \\ & - x_2 q_{02} + y_2 P_{02})] \end{aligned} \tag{26}$$

The above equation indicates that the reduced velocity is yielded from the relative velocity between the ship and ice floe at the impact point in X, Y, Z directions

$$\left.\begin{array}{r} v_{rel} = (v_0 - y_1 r_0 + z_1 q_0) - (v_{02} - y_2 r_{02} + z_2 q_{20}) \\ u_{rel} = (u_0 + x_1 r_0 - z_1 p_0) - (u_{02} + x_2 r_{02} - z_2 p_{02}) \\ w_{rel} = (w_0 - x_1 q_0 + y_1 P_0) - (w_{02} - x_2 q_{02} + y_2 P_{02}) \end{array}\right\} \tag{27}$$

All velocity components in the six degrees of freedom (DoFs) are complex and include phase information. Consequently, the phase difference between the velocities of different structures is incorporated into the calculation of the reduced velocity. This approach results in a complex reduced velocity, v_{rel}, which's RAO is utilized in the calculation of stochastic mean for evaluating ice loads.

Fig. 6 depicts the Response Amplitude Operator (RAO) of relative velocity in X, Y, Z directions between the ship and ice at the point of impact immediately before the collision. It is important to note that the

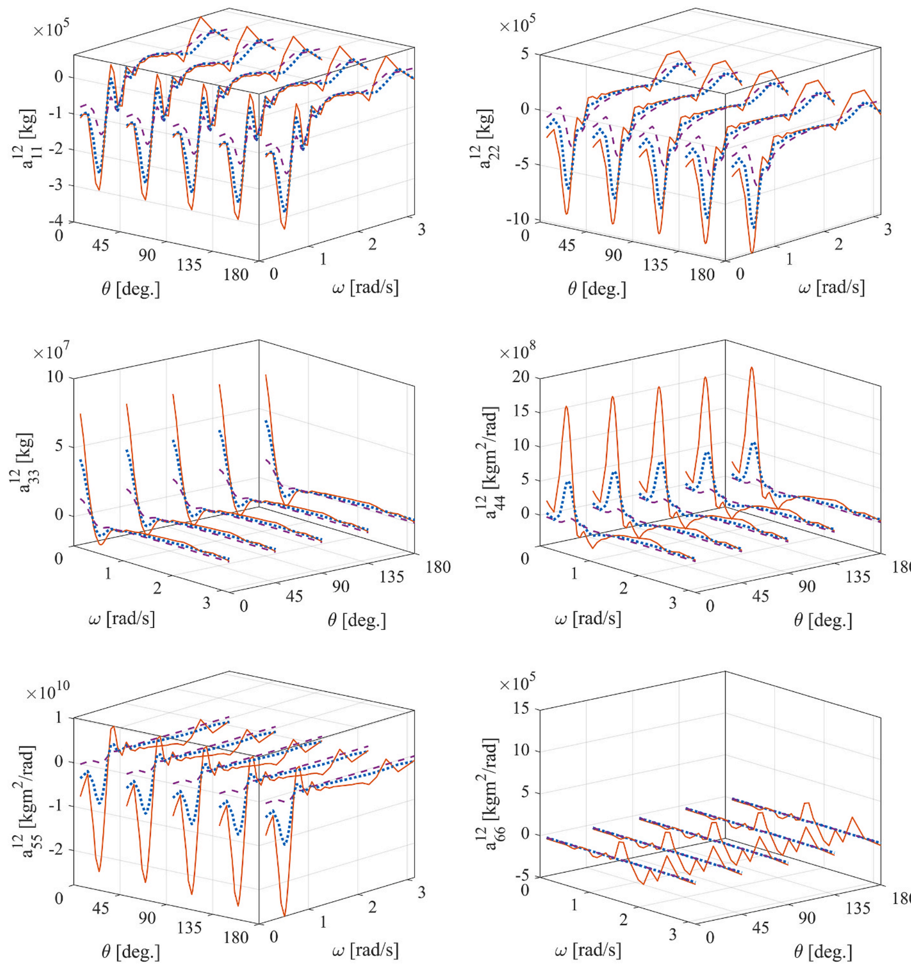

Fig. 9. RAO of added mass acting on the ship due to the ship-ice hydrodynamic interaction in six DoFs, dashed curves indicate the small ice floe, $D_i = 0.3L_{oa}$, dotted curves indicate the medium ice floe, $D_i = 0.6L_{oa}$, solid curves indicate the large ice floe, $D_i = 0.9L_{oa}$.

ship's forward speed is excluded from the surge relative velocity calculation, focusing instead on the impact of sea waves and hydrodynamic interaction on the motions of both ship and ice. Conversely, the ship's advancing speed is factored into the evaluation of the stochastic mean in sea states, as shown in Fig. 7.

In Fig. 6, each curve exhibits a pronounced peak at or below 1 rad/s, indicating the motions of the vessel and ice are highly sensitive to wave frequency, with RAO values significantly diminishing for frequencies above 2 rad/s. This sensitivity underscores the dynamic response of both the vessel and ice to varying wave frequencies. Despite the consistency in peak locations across different wave directions, the peak values markedly vary with wave direction changes, highlighting the influence of both the vessel's geometry and the hydrodynamic interaction with the ice floe on motion sensitivity. It is well recognized that the ship's motions are sensitive to the wave direction because its hull is not rotational symmetry. Although the ice floe's circular geometry would suggest insensitivity to wave direction when floating independently, the presence of hydrodynamic interactions modifies its behavior, making it susceptible to wave direction as noted by Jiang et al. (2023). As a result, the wave direction shows a strong effect on the relative velocity. Furthermore, the impact of ice floe size on relative velocity is less significant compared to sea waves, with varying influence across different motions. This might be attributed to the ice floe's geometry, which tends to distribute the ice floe's volume extensively in the horizontal plane. As a result, a significant portion of the volume is located far from the ship, thereby diminishing the effect of ice floe size on the motions.

Utilizing the wave spectrum, the stochastic mean of reduced velocity is determined as outlined in Equation (8). Fig. 7 displays the mean reduced velocity across different sea states, computed using Equations (8), (13) and (24). Consistent with prior observations, relative velocity exhibits limited sensitivity to ice floe size, a trend also mirrored in the reduced velocity shown in Fig. 7. Here, the black dash-dotted line signifies the reduced velocity induced solely by the ship's forward speed in calm waters, illustrating a pronounced increase in reduced velocity due to sea waves. This amplification correlates directly with the significant wave height and inversely with the sea state's peak period, highlighting a greater impact of wave height over peak period. Notably, at a peak period of 7.7 s, curve fluctuations are most pronounced, indicating that wave direction's influence varies with the sea state's peak period. Fig. 6's peak locations around 1 rad/s align closely with the wave spectra for sea states at a 7.7 s peak period, as depicted in Fig. 5, accentuating wave direction's effect on relative velocity and contributing to Fig. 7's curve fluctuations. The alignment of peaks between the relative velocity curves and wave spectra curves leads to an inverse correlation between the amplitude of reduced velocity and the peak period of the wave spectra, as explained by Equation (8). The relationships between relative velocity and significant height, as well as between relative velocity and peak period, highlight the strong connections between the dynamics of relative velocity and the characteristics of wave spectra. In addition, Fig. 6 indicates that the peak of the reduced velocity curve for the ice floe with $D_i = 0.3L_{oa}$, occurs at $\theta = 90^\circ$ whereas the highest peaks for the ice floes with $D_i = 0.6L_{oa}$, and $D_i = 0.9L_{oa}$, locate at $\theta = 135^\circ$. Alike, the peaks of the three ice floes, with diameters $D_i = 0.3L_{oa}$, $D_i = 0.6L_{oa}$, and $D_i = 0.9L_{oa}$, are also found

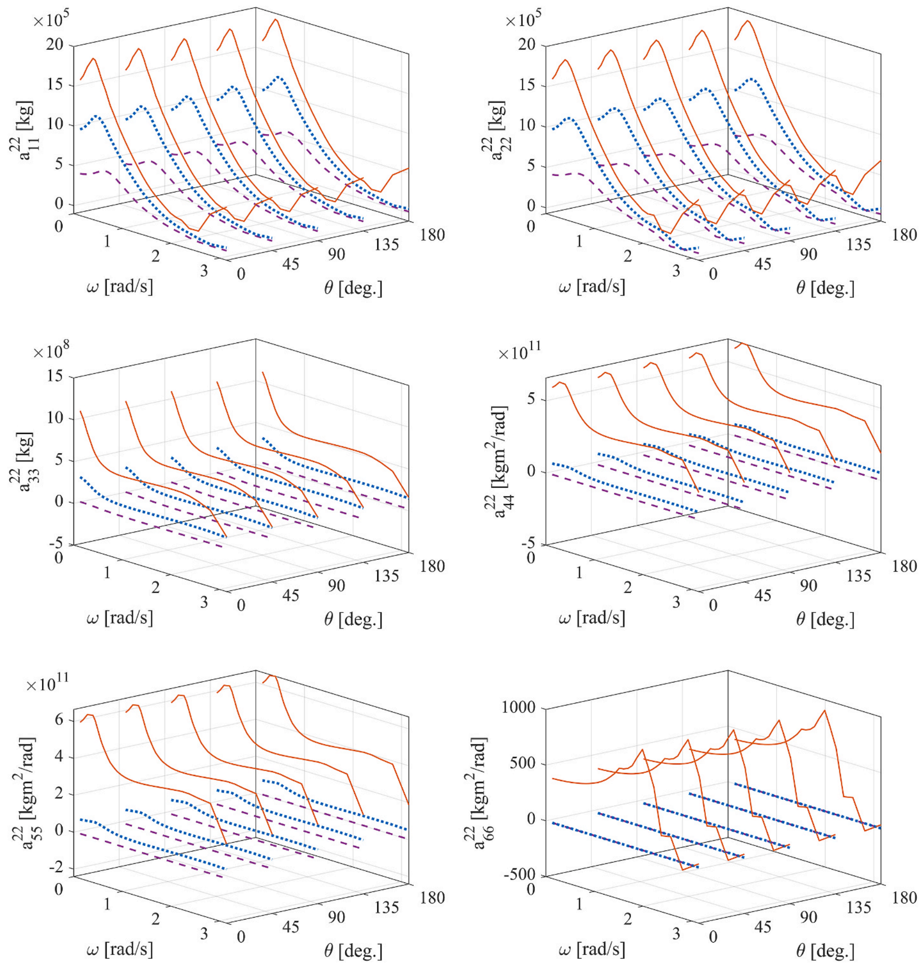

Fig. 10. RAO of ice floes' added mass induced by their own oscillation in six DoFs, dashed curves indicate the small ice floe, $D_i = 0.3L_{oa}$, dotted curves indicate the medium ice floe, $D_i = 0.6L_{oa}$, solid curves indicate the large ice floe, $D_i = 0.9L_{oa}$.

at $\theta = 90^\circ, 135^\circ, \textit{and}\ 135^\circ$, respectively. This pattern aligns with the understanding that a floating body's response in a given sea state can be predicted by its Response Amplitude Operators (RAOs).

4.2. Added mass and reduced mass

Traditional ice load evaluation relies on empirical and analytical formulas for determining added mass, often overlooking the effects of geometry, sea waves, and hydrodynamic interactions between the ship and ice. For instance, Dolny (2018) introduced formulas to compute the added mass coefficients for ships, focusing solely on the main dimensions and form coefficients of the ship's hull. The added mass coefficients for ice are further simplified to constants. Refer to Table 2, where C_{wp} is the waterplane coefficient, C_b is the block coefficient. In the current research, reduced mass is determined by $a_{kj}^{11} + a_{kj}^{12}$ for the ship and $a_{kj}^{21} + a_{kj}^{22}$ for the ice floe, incorporating the influence of geometry and sea waves. The terms a_{kj}^{12} and a_{kj}^{21} specifically represent the hydrodynamic interactions.

Fig. 8 presents the Response Amplitude Operator (RAO) of the ship's added mass resulting from its oscillations in six Degrees of Freedom (DoFs). As dictated by Equation (4), the encounter frequency changes with wave direction, leading to varying encounter frequencies for different wave directions, even when the incoming wave frequency remains the same. Consequently, the added mass curves differ across various wave directions, highlighting the significant impact of wave frequency and direction—an aspect entirely overlooked by empirical formulas. Since $a_{ii}^{11}, i = 1, 2, \ldots, 6$, represent the added mass induced by the oscillation of ship, the effect of ice floe size is not discernible in Fig. 8.

Fig. 9 presents the RAO curves for the added mass on the ship resulting from ship-ice hydrodynamic interactions across six Degrees of Freedom (DoFs). The added mass $a_{ii}^{12}, i = 1, 2, \ldots, 6$, originate from the ship-ice hydrodynamic interaction, illustrating a clear influence of ice floe size. The degree of influence is directly related to the size of the ice, with its significance varying across different DoFs. As illustrated, this effect is more pronounced in vertical DoFs (heave, roll, pitch), while it is less marked in horizontal DoFs (surge, sway, yaw). In surge, sway, and pitch, a notable trough in the curves indicates a reduction in added mass due to hydrodynamic interactions, whereas an increase is observed in heave and roll, as evidenced by peaks in the added mass curves. In yaw, the added mass's absolute value is considerably lower compared to other DoFs, attributed to the circular geometry of the ice floe, which results in minimal radiation in yaw, thereby diminishing the hydrodynamic interaction. Furthermore, the wave direction does not show an evident effect on $a_{ii}^{12}, i = 1, 2, \ldots, 6$. This is because the ice floe is free-floating without any advancing speed.

Fig. 10 displays the RAO of the added mass for ice floes, triggered by their oscillations across six Degrees of Freedom (DoFs). Given the immobility of ice floe, it follows that the wave direction has no influence on the added mass $a_{ii}^{22}, i = 1, 2, \ldots, 6$. In contrast, the size of the ice floes significantly influences the added mass, as the added mass results from the floes' oscillations. The distribution of the ice floe's volume, predominantly in the horizontal dimension with a diameter substantially

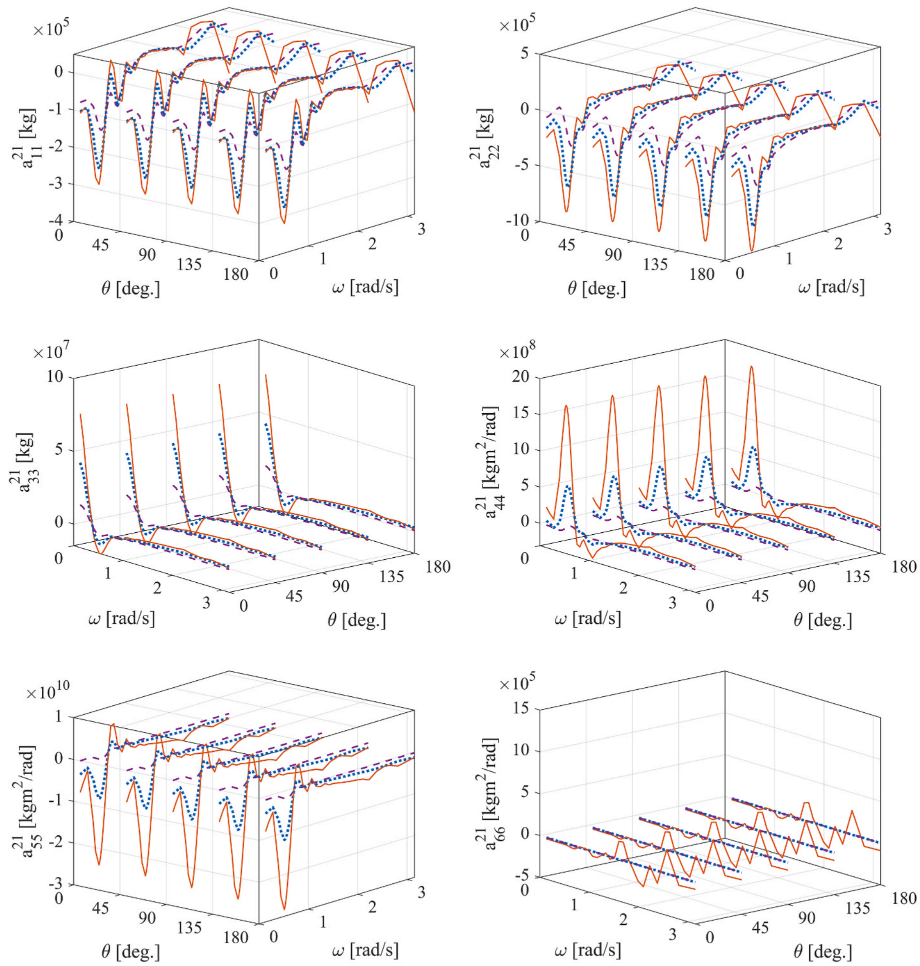

Fig. 11. RAO of added mass acting on ice floes due to the ship-ice hydrodynamic interaction in six DoFs, dashed curves indicate the small ice floe, $D_i = 0.3L_{oa}$, dotted curves indicate the medium ice floe, $D_i = 0.6L_{oa}$, solid curves indicate the large ice floe, $D_i = 0.9L_{oa}$.

exceeding its thickness, markedly affects the added mass in various DoFs. For example, a_{33}^{22} is notably larger than a_{11}^{22} and a_{22}^{22} by three orders of magnitude. a_{66}^{22}, in contrast, exhibits minimal absolute values relative to the added mass in other DoFs, attributable to the ice floe's circular geometry, a factor previously noted.

Fig. 11 illustrates the RAO curves of the added mass on ice floes resulting from ship-ice hydrodynamic interactions across six Degrees of Freedom (DoFs). A comparison between the curves in Figs. 9 and 11 reveals that $a_{ii}^{12} \approx a_{ii}^{21}, i = 1, 2, \ldots, 6$, suggesting a reciprocal interaction between the ship and ice, a finding supported by Gurjev (1997). Further analysis of the absolute values of a^{22} and a^{21} reveals that the hydrodynamic interaction's effectiveness varies across different DoFs. For example, a_{22}^{22} and a_{22}^{21} are of same magnitude, whereas a_{44}^{22} exceeds a_{44}^{21} with approximately three orders of magnitude, suggesting a more pronounced impact of hydrodynamic interactions on the ice's added mass in sway.

Fig. 12 presents the stochastic mean of the ship's added mass with the effect of ship-ice hydrodynamic interaction across six Degrees of Freedom (DoFs). Compared to added mass values derived from empirical formulas, incorporating sea waves generally increases the evaluated added mass. This increase correlates with the significant wave height of the wave spectrum, whereas the peak period's impact is less significant. The influence of wave direction becomes notable only in sea states with a peak period of 7.7 s. The effect of ice floe size varies across the six DoFs: its effect is weak in surge, sway, and yaw, yet substantial in heave, roll, and pitch. An intriguing observation is that the ship's added mass in heave and roll escalates with the size of the ice floe, whereas it slightly diminishes with ice floe size increase in pitch. This variation in influence likely stems from the ice floe's geometry, which is predominantly distributed in horizontal dimensions, rendering the influence less marked in horizontal DoFs (surge, sway, and yaw) compared to vertical DoFs (heave, roll, and pitch). Moreover, the influence is most pronounced in roll, a DoF where a ship's added mass is typically minimal due to the hull's transverse section's near half-circle shape. Correspondingly, the peak value of a_{44}^{12} is approximately 2.5 times that of a_{44}^{11}, as shown in Figs. 8 and 9, illustrating the hydrodynamic interaction's role in determining the effect of ice floe on added mass evaluations of ship in roll. The reduction in pitch added mass across varying ice floe sizes highlights the impact of hydrodynamic interaction: as ice floe size increases, the negative values of a_{55}^{12} become more significant in absolute terms. This trend yields smaller values of $a_{55}^{11} + a_{55}^{12}$ with increasing ice floe size, ultimately resulting in a diminished stochastic mean of pitch added mass.

Fig. 13 displays the stochastic mean of ice floes' added mass with the effect of ship-ice hydrodynamic interaction across six Degrees of Freedom (DoFs). The inclusion of sea waves and hydrodynamic interactions generally elevates the added mass in five DoFs, with the exception of yaw. This exception can be linked to the circular geometry of the ice floe, which leads to near-zero evaluations by the potential flow method, contrasting with empirical formulas that do not consider the ice floe's geometry, thus yielding higher evaluations. The data in Fig. 13 reflects ice floe motions, making the added mass directly proportional to the ice floe's size. The curves show minimal fluctuation with wave direction, indicating a negligible impact of wave direction on ice floe

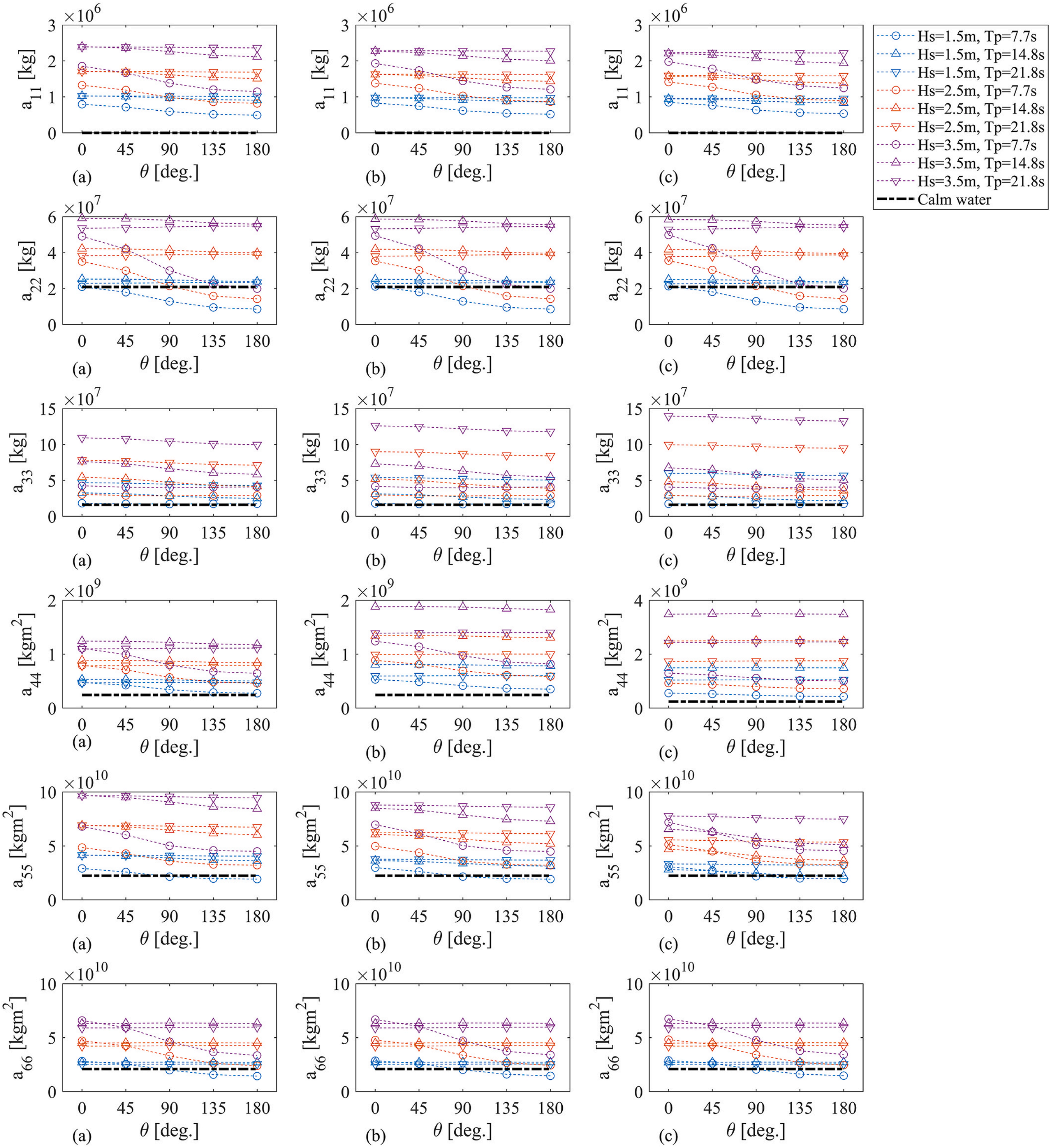

Fig. 12. Mean of ship's added mass with the effect of ship-ice hydrodynamic interaction in six DoFs, the black dash-dotted line represents the results deriving from empirical formulae, column (a), (b), and (c) represent the small ice floe $D_i = 0.3L_{oa}$, medium ice floe $D_i = 0.6L_{oa}$, and large ice floe $D_i = 0.9L_{oa}$, respectively.

added mass due to the ice floe's free-floating condition. Similar to the ship, the significant wave height exerts a more substantial effect on the added mass than the peak period of the wave spectrum. Furthermore, the hydrodynamic interaction's impact inversely correlates with the ice floe's size, as seen in the comparison between roll and pitch added mass. Given the ice floe's geometry possesses infinite orders of rotational symmetry, the added mass in roll and pitch would be identical in the absence of nearby bodies. However, a_{44} significantly exceeds a_{55} in column (a) of Fig. 13, with the discrepancy reducing from column (a) to (c). This trend suggests a diminishing effect of ship-ice hydrodynamic interaction as ice floe size increases.

4.3. Ice loads in regular waves

Conducting research in regular waves is both worthwhile and valuable as it offers insights into the influence of wave dynamics on ice loads

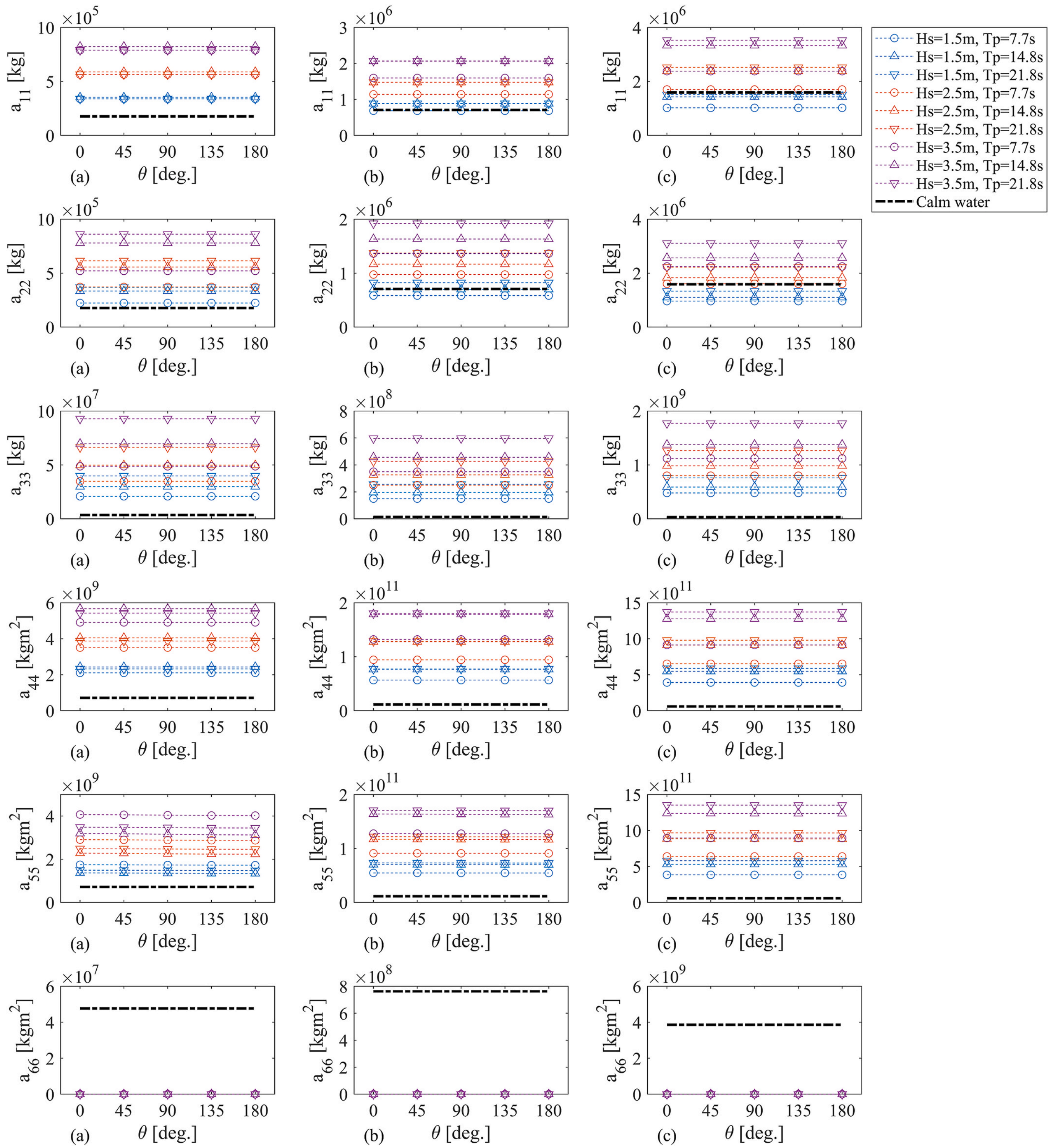

Fig. 13. Mean of ice floe's added mass with the effect of ship-ice hydrodynamic interaction in six DoFs, the black dash-dotted line represents the results deriving from empirical formulas, column (a), (b), and (c) represent the small ice floe $D_i = 0.3L_{oa}$, medium ice floe $D_i = 0.6L_{oa}$, and large ice floe $D_i = 0.9L_{oa}$, respectively.

under relatively simple conditions. This helps to separately demonstrate the influence of wave parameters, such as wave height, wave frequency, and wave direction. As shown in Fig. 14, the computations in regular waves with 1.5 m wave height in beam sea were first verified by comparing them with the conventional Popov method. Fig. 14 indicates a peak around 0.8 rad/s, where the ice loads from the present model are larger than those from the Popov method. In other regions, the ice loads are similar to those predicted by the Popov method. The increased ice loads observed in the peak region can be attributed to wave-induced motions, as evidenced by the correspondence between the peak locations of ice loads and reduced velocity. Additionally, the alignment of both curves suggests that as wave-induced motions increase the reduced velocity, they consequently enhance the kinetic energy involved, leading to larger ice loads. When the reduced velocity decreases, the ice loads predicted by the present model tend to align with those estimated by the conventional Popov method. This alignment suggests that the

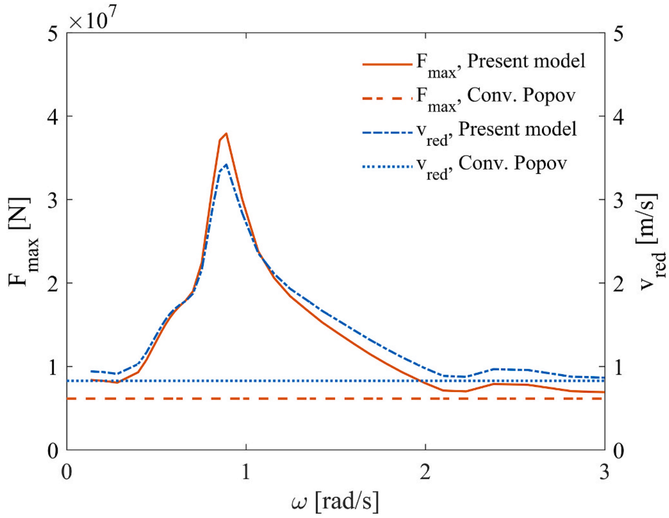

Fig. 14. Comparison of reduced velocity and ice loads between the present model and conventional Popov method in regular waves, $\theta = 90^{\circ}$, $D_i = 0.3L_{oa}$.

present model's evaluations are consistent with the traditional Popov method when the effect of waves is minimal. Therefore, it can be concluded that the present model is effective in evaluating ice loads at the same level as the Popov method while incorporating the influence of wave effects.

Fig. 15 presents ice loads induced by ship-ice glancing impacts in regular waves with three wave heights, indicating the influence of wave frequency, wave direction, wave height, and ice size. The effect of wave frequency is clearly demonstrated, with pronounced peaks located between 0.5 and 1 rad/s. The location of these peaks corresponds to the reduced velocity in Fig. 6, indicating that the increase is mainly due to wave-induced velocity. Fig. 15 also demonstrates the effect of wave direction by showing the various ice loads at the same wave frequency but in different wave directions. For example, the peaks of ice load curves have different values in different directions. The wave height significantly influences ice loads, with a direct proportionality observed between wave height and ice load. Within the employed ship-ice hydrodynamic interaction model, the reduced velocity increases linearly with wave height. Thus, higher wave height leads to greater kinetic energy inputted into impact, as illustrated in Fig. 16, leading to larger ice loads. Additionally, the size of the ice floe plays a critical role in determining ice loads. Fig. 15 shows that the ice loads are directly

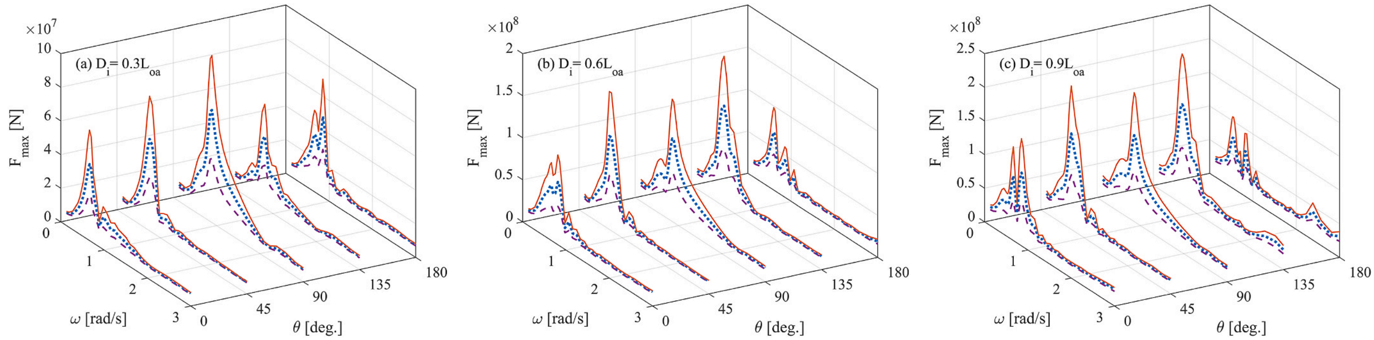

Fig. 15. Ice loads in regular waves induced by impact between ship and ice floes, dashed curves indicate wave height $H = 1.5m$, dotted curves indicate wave height $H = 2.5m$, solid curves indicate wave height $H = 3.5m$.

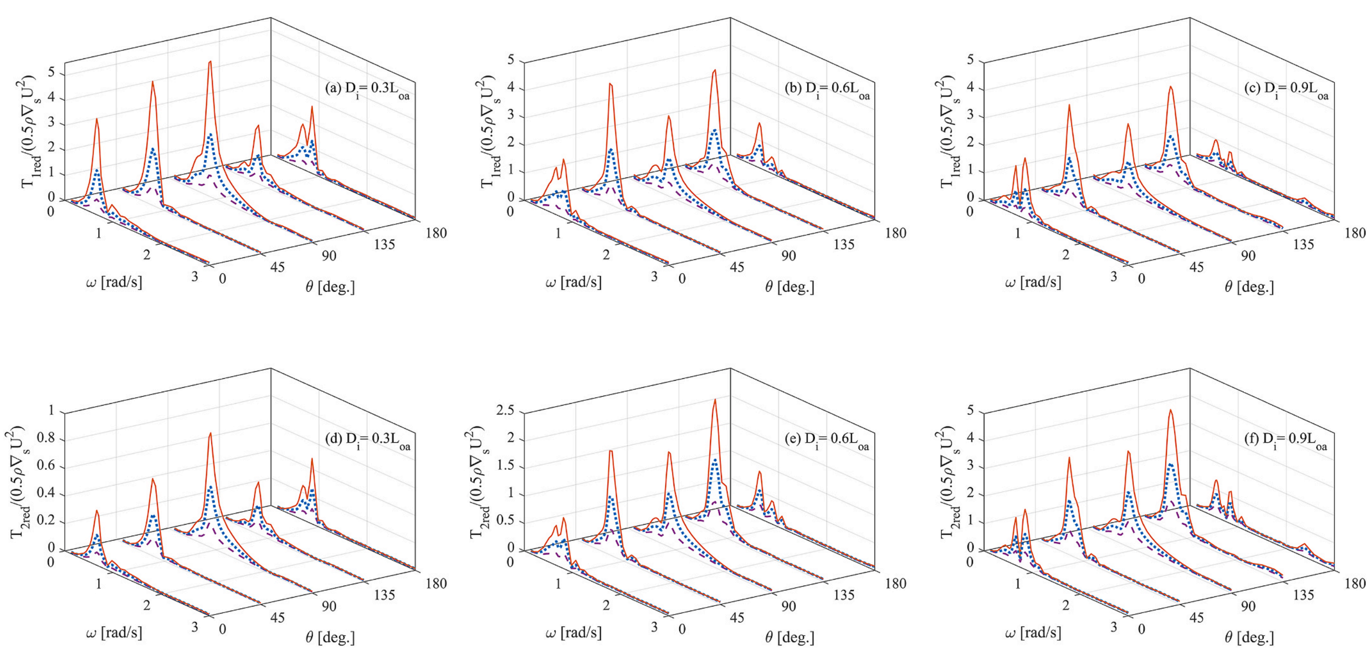

Fig. 16. Kinetic energy of ship (T_{1red}) and ice floes (T_{2red}) reduced in line of impact, ρ is the water density, ∇_s is the displacement of ship, U is the ship speed, dashed curves indicate wave height $H = 1.5m$, dotted curves indicate wave height $H = 2.5m$, solid curves indicate wave height $H = 3.5m$.

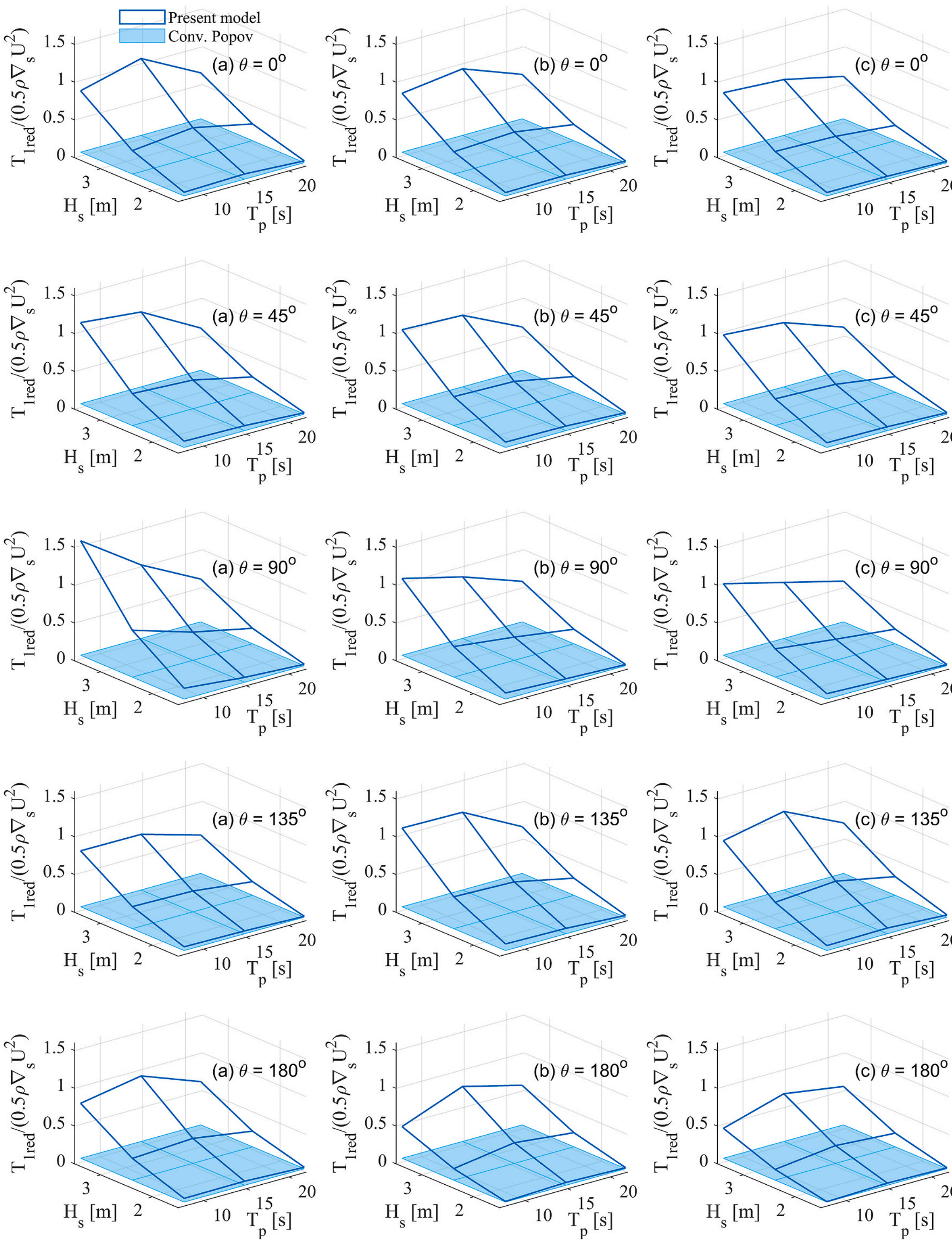

Fig. 17. Kinetic energy of ship reduced in line of impact, ρ is the water density, ∇_s is the displacement of ship, U is the ship speed, columns (a), (b), (c) represents impact with the small ice floe $D_i = 0.3L_{oa}$, medium ice floe $D_i = 0.6L_{oa}$, and large ice floe $D_i = 0.9L_{oa}$, respectively.

proportional to the size of the ice floe. Larger ice floes have greater mass and added mass, as predicted in Figs. 10 and 11, resulting in more kinetic energy being consumed by the ship-ice impact (Fig. 16) and consequently generating larger ice loads. Fig. 16 indicates that the kinetic energy of the ship does not vary as significantly as that of ice floe at the same wave frequency and direction in the impact with different ice floes. In the hydrodynamic interaction between ship and ice floes, different ice floes exert different hydrodynamic effects on the ship, resulting in different response of ship in the identical wave conditions. The variation is weak because the ship's hydrodynamic behavior is dominated by its own hydrodynamic properties. This can be uncovered in the comparison of added mass coefficients a^{11}, a^{12}, a^{21}, and a^{22}. In contrast, the variation in the ice floes' kinetic energy is more substantial, primarily due to the change in ice floe size. This significant fluctuation underscores the substantial impact of ice floe size on the dynamic interactions and resultant ice loads in maritime environments.

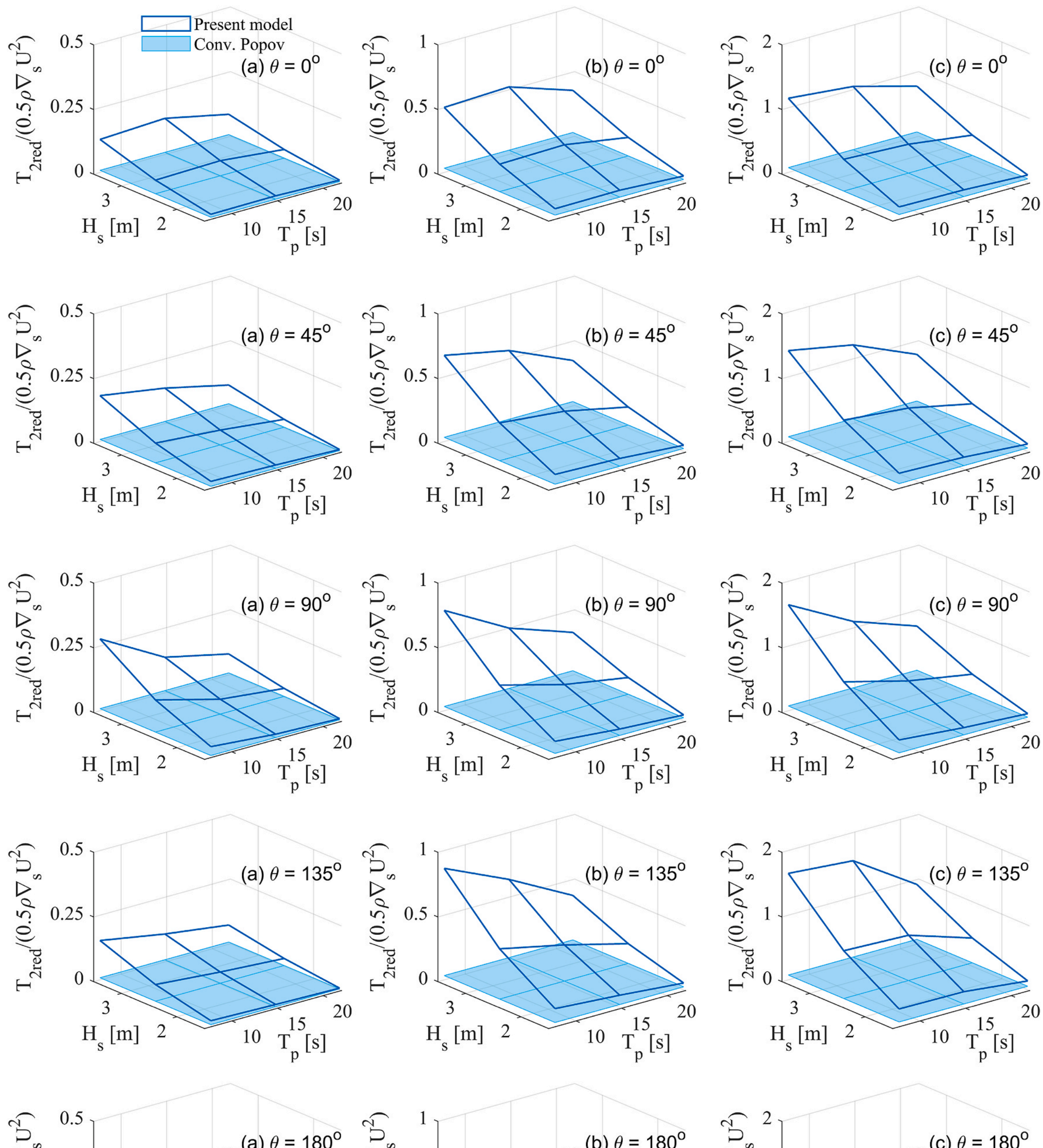

Fig. 18. Kinetic energy of ice reduced in line of impact, ρ is the water density, ∇_s is the displacement of ship, U is the ship speed, columns (a), (b), (c) represents impact with the small ice floe $D_i = 0.3L_{oa}$, medium ice floe $D_i = 0.6L_{oa}$, and large ice floe $D_i = 0.9L_{oa}$, respectively.

4.4. Kinetic energy in sea states

The energy-based evaluation of ice loads operates under the premise that the kinetic energy is expended in the work of the ice load, establishing a direct correlation between the kinetic energy of the ship and ice floe and the amplitude of ice load. This section aims to illustrate how the kinetic energy of the ship and ice floe, reduced in the line of impact across various sea states, varies under the influence of sea waves and ship-ice hydrodynamic interaction.

Fig. 17 demonstrates how the ship's reduced energy during collisions with different ice floes changes across various sea states. Notably, the ship's reduced energy is generally higher when sea waves and hydrodynamic interaction are accounted for. This increase is logical, as wave-induced motions raise the reduced velocity (see Fig. 7). Moreover, the ship's added mass tends to be greater with the consideration of sea waves and hydrodynamic interaction (as shown in Fig. 12). The influence of significant wave height on ice loads is more pronounced than that of the peak period, as indicated by the gradient of ice loads across

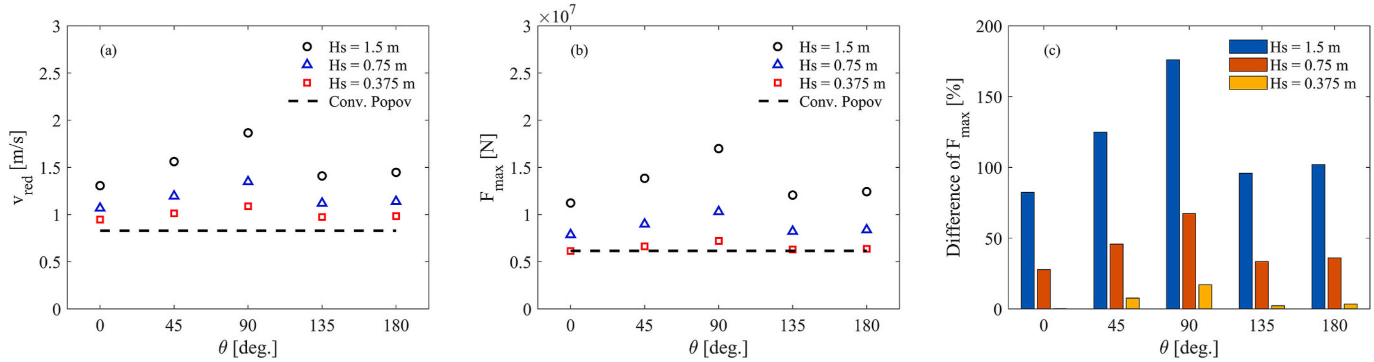

Fig. 19. Comparison of reduced velocity and ice loads between Popov method (dashed line) and present approach (dots) at various sea states: (a) magnitude of reduced velocity, (b) magnitude of ice load, (c) percentage difference of ice load.

different sea states. While wave direction does affect the magnitude of ice loads, its impact is less significant compared to significant wave height and peak period, and this influence diminishes with longer peak periods. The ice floe size has a weak impact on ice loads, which varies depending on sea wave conditions. For instance, ice load fluctuations are more significant in sea states with $H_s = 3.5m, T_p = 7.7s$ compared to other sea states.

Fig. 18 displays the reduced energy of ice floes during collisions with the ship across various sea states, clearly showing that the ice floe's reduced energy is directly proportional to its size. This correlation arises because both the mass and added mass of the ice floe, as evidenced in Fig. 13, increase with its size, whereas the reduced velocity remains relatively stable, as indicated in Fig. 7. Similarly to the ship's reduced energy, the inclusion of sea wave effects notably elevates the ice floe's reduced energy. This increase directly correlates with significant wave height and inversely with peak period. The effect of wave direction on the ice floe's reduced energy mirrors its impact on the ship's reduced energy, with the most significant influence observed in the sea state with $H_s = 3.5m, T_p = 7.7s$.

4.5. Ice loads in sea states

This section utilizes an energy-based model, originally proposed by Popov et al. (1967), for the assessment of ice loads, incorporating considerations of added mass and wave-induced motions. Unlike the original formulation by Popov et al., which does not account for the effects of sea waves and ship-ice hydrodynamic interactions - resulting in an assumption of uniform added mass across different sea states and an oversight of motions beyond the ship's forward advancement - this updated application integrates these elements. The presentation of results using the traditional Popov method serves two purposes: (1) to validate the outcomes of the current model, and (2) to elucidate the significant influence of sea waves and ship-ice hydrodynamic interactions on ice load evaluations. As the significant wave height decreases, the ice loads evaluated by the present model should approach those derived from the Popov method. Therefore, reduced velocity and ice loads are calculated at three significant wave heights ($H_s = 1.5m$, $0.75m, 0.375m$) and an identical peak period ($T_p = 7.7s$), as shown in Fig. 19. Fig. 19 demonstrates that the present model's predictions converge with those of the Popov method as significant wave height decreases, indicating the reliability of the present approach. Furthermore, this trend verifies that the present approach effectively reflects the influence of waves on ice load evaluation.

Fig. 20 illustrates ice load calculations using the current model across various sea states and compares these to evaluations made with the conventional Popov method. The Popov method, lacking consideration for sea wave effects, produces uniform evaluations across different sea states, reflected as flat surfaces in each subplot of Fig. 20. Conversely, the current model reveals a pronounced impact of sea waves on ice loads. Typically, the influence of sea waves on ice loads directly correlates with the significant wave height of the sea states and inversely with the peak period. The ice loads predicted by the new model align with those of the conventional Popov method as the significant wave height decreases, indicating that the new model can accurately forecast ice loads similar to the conventional method under conditions of minimal wave amplitude. The effect of wave direction is substantially less significant than that of significant wave height and peak period. This lesser influence of wave direction can be attributed to the ice floe's free-floating condition and its rotational symmetry, leading to reduced velocity (as illustrated in Fig. 7) and ice floe added mass (as shown in Fig. 13) being largely unaffected by wave direction, thereby minimally impacting calculated ice loads. Both the conventional Popov method and the current model concur that ice loads increase with the size of the ice floe. This is a logical outcome since larger ice floes impart more kinetic energy during ship-ice collision, resulting in higher ice loads.

According to Equation (22), the ice load magnitude depends on the reduced mass (M_{red}) and reduced velocity (v_{red}) with given ice floe's geometry and crushing strength. To explore the correlation of ice load – reduced mass and ice load – reduced velocity, we present the scatter plots of ice loads (F_{max}) as a function of reduced mass (Fig. 21a) and reduced velocity (Fig. 21b), respectively. The correlation between two sets of data can be measured with Pearson Correlation Coefficient (γ)

$$\gamma = \frac{\sum_{i=1}^{n}(x_i - \bar{x})(y_i - \bar{y})}{\sqrt{\sum_{i=1}^{n}(x_i - \bar{x})^2 \sum_{i=1}^{n}(y_i - \bar{y})^2}} \tag{28}$$

where x and y represent data sets 1 and 2, respectively, n is the data count. Herein, Pearson Correlation Coefficient is employed to investigate the correlations: 1) between M_{red} and F_{max}, and 2) between v_{red} and F_{max}, respectively. Table 3 presents the Pearson Correlation Coefficients of $M_{red} - F_{max}$ (γ_1) and $v_{red} - F_{max}$ (γ_2) against different ice floe sizes. It shows that $\gamma_2 > \gamma_1$, which indicates a stronger correlation between reduced velocity and ice loads. The reduced mass is determined by the mass and added mass while the reduced velocity is affected by the wave induced motions. This suggests wave-induced motions exert a more significant influence on ice loads. The strong correlation between reduced velocity and ice loads, reflected by γ_2 being close to 1, is consistent across different ice floe sizes, implying that ice floe size does not significantly affect the relationship. In contrast, the variability of γ_1 across the ice floe sizes suggests a stronger effect of ice floe size on the correlation between the reduced mass and ice loads. Furthermore, Fig. 21 illustrates that ice loads are grouped based on significant wave heights, which have a proportional relationship with ice loads, highlighting the substantial influence of significant wave heights on ice loads. An intriguing observation is the increased dispersion of ice loads relative to reduced mass (Fig. 21a) and reduced velocity (Fig. 21b) with

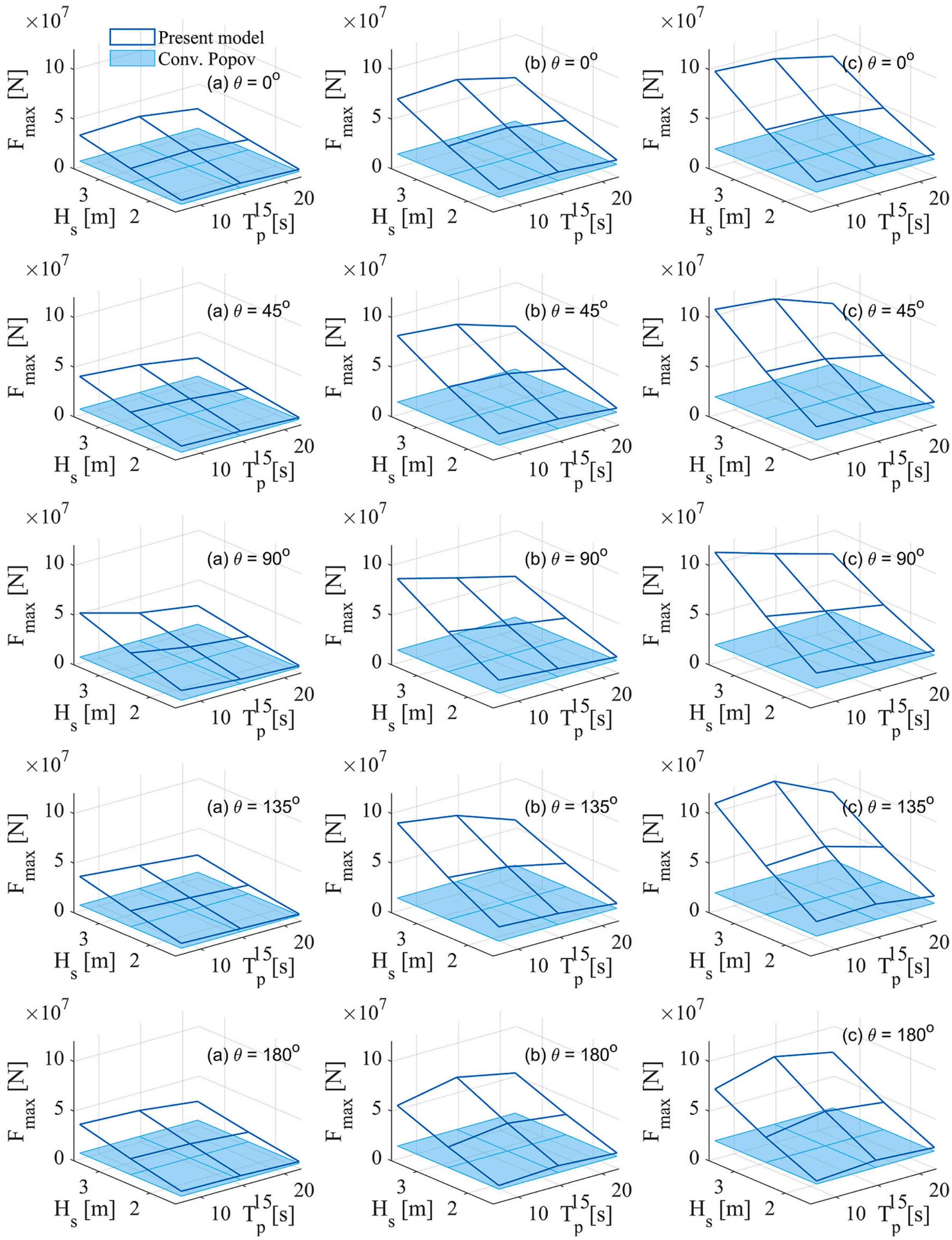

Fig. 20. Ice loads evaluated with present model in various sea states and conventional Popov method without considering the sea waves, column (a), (b), and (c) represent impact with the small ice floe $D_i = 0.3L_{oa}$, medium ice floe $D_i = 0.6L_{oa}$, and large ice floe $D_i = 0.9L_{oa}$, respectively.

rising significant wave heights. The dispersion between groups is larger than that within each group, which is caused by the peak period and wave direction. This suggests that higher significant wave heights contribute to greater variability in ice loads, reflecting the complex interplay between wave dynamics and ice load evaluations. Moreover, Fig. 21 demonstrates that the proposed model and the conventional Popov method yield identical correlations between reduced mass and ice loads (Fig. 21a), as well as reduced velocity and ice loads (Fig. 21b). This similarity provides positive verification of the proposed model.

5. Conclusions and future work

The research presented in this manuscript offers a comprehensive analysis of the influence of hydrodynamic interactions and wave-induced motions on the evaluation of ice loads during ship-ice collisions in wave environments. A newly proposed potential flow method is

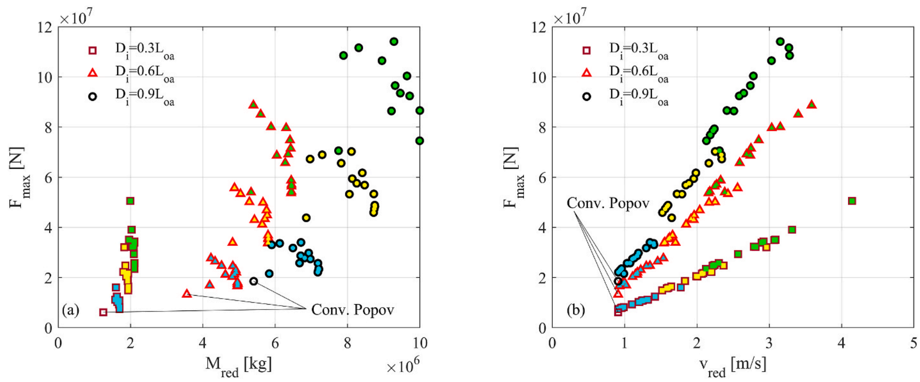

Fig. 21. Scatter plots of ice loads as a function of (a) reduced mass and (b) reduced velocity, color cyan denotes the sea states with 1.5 m significant wave height, color yellow denotes the sea states with 2.5 m significant wave height, color green denotes the sea states with 3.5 m significant wave height.

Table 3
Pearson's correlation coefficients of $M_{red} - F_{max}$ (γ_1) and $v_{red} - F_{max}$ (γ_2).

Ice floe	γ_1	γ_2
$D_i = 0.3L_{oa}$	0.752	0.997
$D_i = 0.6L_{oa}$	0.701	0.992
$D_i = 0.9L_{oa}$	0.738	0.989

introduced to calculate the hydrodynamic interaction between an advancing ship and a free-floating ice floe. The influence of sea waves is analyzed by introducing random sea waves with various significant wave heights, peak periods, and wave directions. Key conclusions from this study include.

(1) Hydrodynamic interaction significance: The study demonstrates that hydrodynamic interactions between the ship and ice significantly affect the evaluation of ice loads. These interactions were found to modify the added mass and motion responses of both ship and ice in six degrees of freedom, which are critical factors in the accurate prediction of ice loads.
(2) Impact of sea waves: The results highlight that waves play a crucial role in influencing ice loads by changing the relative velocity between the ship and ice immediately before the glancing impact, and consequently changes the reduced velocity and kinetic energy involved in the impact. Consequently, sea waves exert a considerable influence on ice loads, emphasizing the importance of accounting for wave dynamics in accurately assessing ice load magnitudes during ship-ice interactions.
(3) Advancements in ice load predictions: By using an improved energy-based method with a newly developed potential flow model, this study indicates that the evaluation of ice loads can be significantly enlarged by accounting for the influence of hydrodynamic interactions and the dynamic effects of sea states. In addition, the correlation between reduced velocity and ice loads is stronger than that between reduced mass and ice loads. The findings emphasize the need for considering hydrodynamic effects and wave conditions in the design and operation of ice-strengthened ships since accurate ice load predictions are essential for ensuring the structural integrity and safety of ships navigating in ice-infested waters.

The current study employs stochastic wave spectra for the determination of added mass and wave-induced motions under various sea states. However, this approach is limited in its capacity to generate the time history curve of ice loads, rendering the analysis of time-varying characteristics of ice loads during ice crushing processes infeasible. The approach also fails to account for the precise impact point, which fluctuates due to wave-induced motions. Additionally, the research presupposes that ice failure occurs solely through crushing, overlooking the multifaceted nature of ice failure mechanisms, which also include splitting and bending, alongside crushing. Incorporating a broader spectrum of failure patterns could significantly enhance the accuracy of ice load assessments. Furthermore, experimental and full-scale testing would further validate the model predictions and contribute to safer and more efficient designs and operation for ice-going ships. The approach in this study is not suitable for scenarios involving continuous ice failures with multiple failing circles, such as the evaluation of level ice resistance. Additionally, this approach does not extend to predicting the ongoing motions of ships and ice after ship-ice impacts, which could be more accurately modeled using a time-domain ship-ice interaction model that incorporates wave effects. These specifications help to clarify the scope and applicability of our findings and sets a clear direction for future research efforts.

CRediT authorship contribution statement

Zongyu Jiang: Writing – original draft, Visualization, Validation, Software, Project administration, Methodology, Investigation, Formal analysis, Data curation, Conceptualization. **Pentti Kujala:** Writing – review & editing, Validation, Supervision, Resources, Methodology, Formal analysis, Data curation, Conceptualization. **Spyros Hirdaris:** Writing – review & editing, Validation, Supervision, Software, Resources, Data curation, Conceptualization. **Fang Li:** Writing – review & editing, Validation, Methodology, Formal analysis, Data curation, Conceptualization. **Tommi Mikkola:** Writing – review & editing, Validation, Supervision, Formal analysis, Data curation. **Mikko Suominen:** Writing – review & editing, Validation, Supervision, Resources, Project administration, Methodology, Investigation, Funding acquisition, Formal analysis, Data curation, Conceptualization.

Declaration of competing interest

The authors declare that they have no known competing financial interests or personal relationships that could have appeared to influence the work reported in this paper.

References

Alberello, A., Bennetts, L.G., et al., 2022. Three-dimensional imaging of waves and floes in the marginal ice zone during a cyclone. Nat. Commun. 13 (1), 4590.
Barooni, M., Nezhad, S.K., Ali, N.A., Ashuri, T., Sogut, D.V., 2022. Numerical study of ice-induced loads and dynamic response analysis for floating offshore wind turbines. Mar. Struct. 86, 103300.

Cheng, S., Rogers, W.E., Thomson, et al., 2017. Calibrating a viscoelastic sea ice model for wave propagation in the Arctic fall marginal ice zone. J. Geophys. Res.: Oceans 122 (11), 8770–8793.
Choi, Y.H., Choi, H.Y., Lee, C.S., Kim, M.H., Lee, J.M., 2012. Suggestion of a design load equation for ice-ship impacts. Int. J. Nav. Archit. Ocean Eng. 4 (4), 386–402.
Daley, C., 1999. Energy based ice collision forces. In: Proceedings of the 15th International Conference on Port and Ocean Engineering under Arctic Conditions (POAC), 2, pp. 674–686.
Daley, C., 2000. IACS Unified Requirements for Polar Ships – Design Ice Loads. IACS Ad-Hoc Group on Polar Class Ships. Memorial University of Newfoundland.
Det Norske Veritas, 2019. Environmental conditions and environmental loads. DNV Classification Note, DNV-RP-C205.
Di, S., Xue, Y., Wang, Q., Bai, X., 2017. Discrete element simulation of ice loads on narrow conical structures. Ocean Eng. 146, 282–297.
Dolny, J., 2018. Methodology for defining technical safe speeds for light ice-strengthened government ships operating in ice. Ship Structures Committee SSC-473.
FSICR, 2017. Ice class regulations and the application of Finnish-Swedish ice class regulations. Helsinki, Finland: Finnish Transport Safety Agency.
Gurjev, Y.V., 1997. Practical application of generalized added masses under interaction of two bodies in fluid. In: Proceedings of 38th Conference, Krylov Readings. St. Petersburg, pp. 251–259.
Hilding, D., Forsberg, J., Gürtner, A., 2011. Simulation of ice action loads on offshore structures. In: Proceedings of the 8th European LS-DYNA Users Conference. Strasbourg.
Idrissova, S., Kujala, P., Repin, R., Li, F., 2019. The study of the Popov method for estimation of ice loads on ship's hull using full-scale data from the Antarctic sea. In: Proceedings of the 25th International Conference on Port and Ocean Engineering under Arctic Conditions, pp. 9–13. Delft, The Netherlands.
Ji, S., Yang, D., 2022. Ice loads and ice-induced vibrations of offshore wind turbine based on coupled DEM-FEM simulations. Ocean Eng. 243, 110197.
Jiang, Z., Li, F., Mikkola, T., Kujala, P., Hirdaris, S., 2022. The influence of added mass in ship-ice-wave interactions: a potential flow hydromechanics model. In: International Conference on Offshore Mechanics and Arctic Engineering, vol. 85864. American Society of Mechanical Engineers. V002T02A027.
Jiang, Z., Li, F., Mikkola, T., Kujala, P., Hirdaris, S., 2023. A boundary element method for the prediction of hydrodynamic ship–ice–wave interactions in regular waves. J. Offshore Mech. Arctic Eng. 145 (6), 061601.
Jiang, Z., Li, F., Tavakoli, S., Kujala, P., Suominen, M., Hirdaris, S., 2024. A viscous investigation on the hydrodynamic coefficients and wave loads under the interaction of side-by-side cylinders in regular waves. Ocean Eng. 297, 117156.
Jordaan, Ian J., 2001. Mechanics of ice-structure interaction. Eng. Fract. Mech. 68, 1923–1960.
Kim, E., Tsuprik, V.G., 2018. Concept of the specific energy of the mechanical destruction of ice versus the ice pressure-area relationship: review and discussion. In: Proceedings of the 24th IAHR International Symposium on Ice Vladivostok, Russia June 4-9, 2018. International Association for Hydro-Environment Engineering and Research (IAHR).
Kotilainen, M., Vanhatalo, J., Suominen, M., Kujala, P., 2017. Predicting ice-induced load amplitudes on ship bow conditional on ice thickness and ship speed in the Baltic Sea. Cold Reg. Sci. Technol. 135, 116–126.
Kujala, P., 1994. On the Statistics of Ice Loads on Ship Hull in the Baltic [doctoral Thesis]. Helsinki University of Technology, Espoo.
Kujala, P., Jiang, Z., Li, F., Lu, L., 2019. Long term prediction of local ice loads on the hull of SA agulhas II. In: Proceedings of the International Conference on Port and Ocean Engineering under Arctic Conditions.
Li, F., Kõrgesaar, M., Kujala, P., Goerlandt, F., 2020. Finite element based meta-modeling of ship-ice interaction at shoulder and midship areas for ship performance simulation. Mar. Struct. 71, 102736.
Li, F., Lu, L., Suominen, M., Kujala, P., 2021a. Short-term statistics of ice loads on ship bow frames in floe ice fields: full-scale measurements in the Antarctic ocean. Mar. Struct. 80, 103049.
Li, F., Suominen, M., Lu, L., Kujala, P., Taylor, R., 2021b. A probabilistic method for long-term estimation of ice loads on ship hull. Struct. Saf. 93, 102130.
Long, X., Liu, S., Ji, S., 2020. Discrete element modelling of relationship between ice breaking length and ice load on conical structure. Ocean Eng. 201, 107152.
Lu, W., Amdahl, J., Lubbad, R., Yu, Z., Løset, S., 2021. Glacial ice impacts: Part I: wave-driven motion and small glacial ice feature impacts. Mar. Struct. 75, 102850.
Lu, W., Lubbad, R., Løset, S., 2014. Simulating ice-sloping structure interactions with the cohesive element method. J. Offshore Mech. Arctic Eng. 136 (3), 031501.
Masterson, D.M., Frederking, R.M.W., Wright, B., Kärnä, T., Maddock, W.P., 2007. A revised ice pressure-area curve. In: Proceedings, Nineteenth International Conf. On Port and Ocean Engineering under Arctic Conditions, vol. 1. Dalian University of Technology Press, Dalian, pp. 305–314.
Muhonen, A., 1991. Medium Scale Indentation Tests—PVDF Pressure Measurements, Ice Face Measurements and Interpretation of Crushing Video. Client Report to National Research Council of Canada, Canadian Hydraulics Center by Helsinki University of Technology, Ship Laboratory. (Accessed 20 February 1991).
Newman, J.N., 2018. Marine Hydrodynamics. The MIT press, p. 448.
Ommani, B., Berthelsen, P.A., Firoozkoohi, R., 2018. Ptil – NORD ST20_2018 Loads, Design and Operation of Floaters in the Arctic.
Passerotti, G., Bennetts, L.G., et al., 2022. Interactions between irregular wave fields and sea ice: a physical model for wave attenuation and ice breakup in an ice tank. J. Phys. Oceanogr. 52 (7), 1431–1446.
Patil, A., Sand, B., Cwirzen, A., Fransson, L., 2021. Numerical prediction of ice rubble field loads on the Norströmsgrund lighthouse using cohesive element formulation. Ocean Eng. 223, 108638.
Polojärvi, A., Tuhkuri, J., Pustogvar, A., 2015. DEM simulations of direct shear box experiments of ice rubble: force chains and peak loads. Cold Reg. Sci. Technol. 116, 12–23.
Popov, Y., Faddeyev, O., Kheisin, D., Yalovlev, A., 1967. Strength of ships sailing in ice. US Army Foreign Science and Technology Center (Translation).
Rahman, M.S., Taylor, R.S., Kennedy, A., Simões Ré, A., Veitch, B., 2015. Probabilistic analysis of local ice loads on a lifeboat measured in full-scale field trials. J. Offshore Mech. Arctic Eng. 137 (4), 041501.
Ranta, J., Polojärvi, A., 2019. Limit mechanisms for ice loads on inclined structures: local crushing. Mar. Struct. 67, 102633.
Riska, K., Rantala, H., Joensuu, A., 1990. Full Scale Observations of Ship–Ice Contact. Helsinki University of Technology, Laboratory of Naval Architecture and Marine Engineering. Report M-97, Espoo, 1990.
Su, B., Riska, K., Moan, T., 2010. A numerical method for the prediction of ship performance in level ice. Cold Reg. Sci. Technol. 60 (3), 177–188.
Su, B., Riska, K., Moan, T., 2011. Numerical study of ice-induced loads on ship hulls. Mar. Struct. 24 (2), 132–152.
Suominen, M., Kujala, P., 2014. Variation in short-term ice-induced load amplitudes on a ship's hull and related probability distributions. Cold Reg. Sci. Technol. 106, 131–140.
Suominen, M., Kujala, P., Romanoff, J., Remes, H., 2017a. Influence of load length on short-term ice load statistics in full-scale. Mar. Struct. 52, 153–172.
Suominen, M., Kujala, P., Romanoff, J., Remes, H., 2017b. The effect of the extension of the instrumentation on the measured ice-induced load on a ship hull. Ocean Eng. 144, 327–339.
Suominen, M., Kõrgesaar, M., Taylor, R., Bergström, M., 2024. Probabilistic analysis of operational ice damage for Polar class vessels using full-scale data. Struct. Saf. 107, 102423, 2024.
Suyuthi, A., Leira, B.J., Riska, K., 2013. Statistics of local ice load peaks on ship hulls. Struct. Saf. 40, 1–10.
Tan, X., Su, B., Riska, K., Moan, T., 2013. A six-degrees-of-freedom numerical model for level ice–ship interaction. Cold Reg. Sci. Technol. 92, 1–16.
Taylor, R.S., Richard, M., Hossain, R., 2019. A probabilistic high-pressure zone model for local and global loads during ice-structure interactions. J. Offshore Mech. Arctic Eng. 141 (5), 051604.
Wang, Q., Li, Z., Lei, R., Lu, P., Han, H., 2018. Estimation of the uniaxial compressive strength of Arctic sea ice during melt season. Cold Reg. Sci. Technol. 151, 9–18.
Weeks, W.F., 1967. The mechanical properties of sea ice. US Army Materiel Command Cold Regions Res. Eng. Lab. 2.
Xu, Y., Kujala, P., Hu, Z., Li, F., Chen, G., 2020. Numerical simulation of level ice impact on landing craft bow considering the transverse isotropy of Baltic Sea ice based on XFEM. Mar. Struct. 71, 102735.
Xu, Y., Wu, J., Li, P., Kujala, P., Hu, Z., Chen, G., 2022. Investigation of the fracture mechanism of level ice with extended finite element method. Ocean Eng. 260, 112048.
Yoon, D.H., Jeong, S.Y., Choung, J., 2023. Collision simulations between an icebreaker and an iceberg considering ship hydrodynamics. Ocean Eng. 279, 114333.
Zhang, M., 2019. Ice Load Prediction for Design of Ice-Going Ships for Inland Waterways. Doctoral dissertation, KTH Royal Institute of Technology.